Published in final edited form as:

Cell Rep. 2025 May 27; 44(5): 115608. doi:10.1016/j.celrep.2025.115608.

LncRNA *SLNCR* phenocopies the E2F1 DNA binding site to promote melanoma progression

Kushani Shah[1,2,3], **Eleni Anastasakou**[1,2,3], **Leinal Sejour**[3,4], **Yufei Wang**[1,2], **Leon Wert-Lamas**[1,2,3], **Christopher Rauchet**[1,2,3,8], **Sabine Studer**[1,2,3,5], **Simon Goller**[1,2,3,9], **Robert J. Distel**[1,2,3], **Wayne Marasco**[1,2], **Lalith Perera**[6], **Ioannis S. Vlachos**[3,4,7], **Carl D. Novina**[1,2,3,10,*]

[1]Department of Cancer Immunology and Virology, Dana-Farber Cancer Institute, Boston, MA, USA

[2]Department of Medicine, Harvard Medical School, Boston, MA 02115, USA

[3]Broad Institute of Harvard and MIT, Cambridge, MA 02141, USA

[4]Department of Pathology, Beth Israel Deaconess Medical Center, Harvard Medical School, Boston, MA 02115, USA

[5]Department of Hematology/Oncology, Boston Children's Hospital, Boston, MA 02115, USA

[6]Genome Integrity and Structural Biology Laboratory, NIEHS, NIH, Durham, NC 27709, USA

[7]Spatial Technologies Unit, Harvard Medical School Initiative for RNA Medicine, Beth Israel Deaconess Medical Center, Boston, MA 02115, USA

[8]Present address: Department of Biochemistry, University of Colorado Boulder, Boulder, CO 80309, USA

[9]Present address: Department of Dermatology, Venereology and Allergology, University Hospital Wurzburg, Wurzburg, Germany

[10]Lead contact

SUMMARY

The long non-coding RNA *SLNCR* and the transcription factor E2F1 are known melanoma oncogenes. We show that *SLNCR* binds to E2F1 to promote the proliferation, invasion, and migration of melanoma cells from the bloodstream into the lungs. Blocking *SLNCR*-E2F1

*Correspondence: carl_novina@dfci.harvard.edu.

AUTHOR CONTRIBUTIONS

K.S. designed, performed, and analyzed proliferation, invasion, mouse extravasation, RNA extraction, RT-qPCR, western blotting, E2F1DBD purification, and R/EMSA experiments. E.A. performed and analyzed DMS probing of SLNCR. L.S. and I.S.V. analyzed RNA-seq data. Y.W. and W.M. helped to design, execute, and analyze mouse studies. L.W.-L. performed the Y3H screen. C.R. and S.G. helped execute RT-qPCR and R/EMSA repeats. S.S. cloned plasmids for E2F1 purification. R.J.D. helped design experiments. L. P. conducted MD simulation experiments. All authors analyzed and interpreted data. C.D.N. conceptualized the study. K.S., E.A., and C.D.N. wrote the manuscript with input from all authors.

DECLARATION OF INTERESTS

C.D.N. is co-founder of AI Proteins, Courage Therapeutics, Dynamic Cell Therapies, Microbial Machines, and NextRNA Therapeutics. C.D.N. is a board of directors (B.O.D.) member and consultant for Dynamic Cell Therapies and Microbial Machines and a consultant for Courage Therapeutics. L.W.-L. and S.S. are co-founders of NextRNA Therapeutics. None of these companies have financial interests resulting from the work in this manuscript.

complex formation without reducing the levels of either *SLNCR* or E2F1 prevents lung extravasation in mice. A 60-nt fragment of *SLNCR* contains two RNA analogs of the E2F1 DNA binding site (BS) in opposite orientations and can form a hairpin RNA that phenocopies the E2F1 DNA BS. Molecular dynamics (MD) simulations and biochemical experiments indicate that this fragment of *SLNCR* binds to the E2F1 DNA-binding domain more effectively than the E2F1 DNA BS. MD simulations predict higher affinity for DNA-E2F1 complex formation but faster kinetics and a greater number of RNA-amino acid contacts for the RNA-E2F1 complex, suggesting that RNA binding to E2F1 is more kinetically favorable.

Graphical Abstract

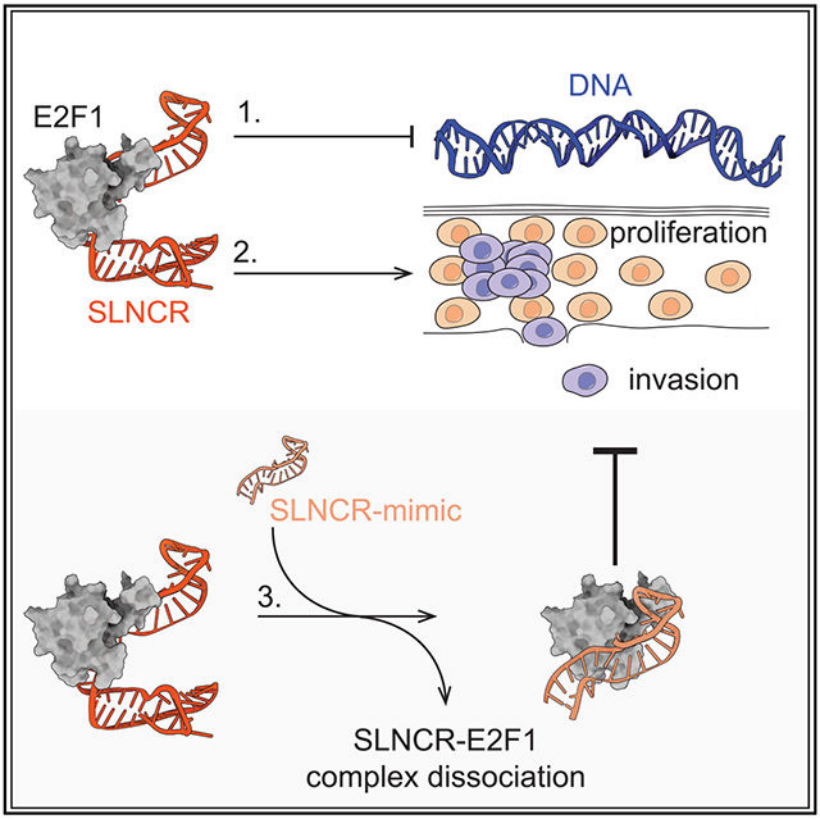

In brief

Shah et al. show that the *SLNCR*-E2F1 complex drives melanoma progression by binding to the E2F1 DNA-binding domain. Blocking *SLNCR*-E2F1 complex formation without changing the levels of either *SLNCR* or E2F1 reduces melanoma invasion and extravasation, suggesting this RNA-protein interaction is a potential target for melanoma therapy.

INTRODUCTION

The E2F family of transcription factors (TFs) are critical for cell cycle regulation.[1] Of the eight family members, E2F1 is the most well studied[2] and has also been implicated in apoptosis, selfrenewal, differentiation, DNA synthesis, DNA damage response, DNA repair,

invasion, and senescence.[2] E2F1 typically binds to DNA as a heterodimer with DP1 or DP2 at E2F1 DNA-binding elements 5′-TTTC[CG]CGC-3′.[1] Although not necessary for DNA binding, DP proteins increase the affinity of and target gene transactivation by E2F1.[1] When overexpressed (e.g., in cancer), E2F1 acts independently of DP proteins to induce apoptosis.[3] In fact, DP1 is dispensable *in vitro* and stabilizes E2F1 binding to promoters in cells.[3,4]

Other proteins that interact with E2F1 can alter its activity. For example, the retinoblastoma (Rb) protein maintains E2F1 in an inactive state. Upon Rb dissociation, E2F1 binds to DNA and transactivates genes.[5] In some cases, E2F1 can bind to DNA in complex with Rb, acting as a transcriptional repressor.[6] E2F1 also interacts with the androgen receptor,[7] with chromatin-modifying proteins such as p300/CBP,[8] and with Tip60.[9] These interactions directly or indirectly regulate E2F1 activity.

E2F1 is a known melanoma oncogene[10] and has been shown to bind to the long non-coding RNA (lncRNA) *SLNCR*,[11,12] which is also a melanoma oncogene.[11,13,14] Most oncogenes are typically identified by genetic alterations such as point mutations, insertions or deletions (indels), copy-number variations, chromosomal translocations, and/or epigenetic changes. Here, we demonstrate that the oncogenic activities of E2F1 and *SLNCR* in melanoma require *SLNCR*-E2F1 complex formation.

TFs may bind RNA through arginine-rich motifs (ARMs) and not their DNA-binding domain (DBD).[15] Using molecular dynamics (MD) simulations to model RNA and DNA binding to the DBD of E2F1 ($E2F1^{DBD}$) and biochemistry, we demonstrate that the double-stranded RNA (dsRNA) binds to and makes more contacts with $E2F1^{DBD}$ compared to dsDNA. Finally, we explore the use of oligonucleotides blocking the *SLNCR*-E2F1 interaction as a novel approach to melanoma therapy.

RESULTS

SLNCR and E2F1 co-regulate melanoma-relevant genes

lncRNAs often modulate TF activities, thereby re-wiring gene regulatory networks.[16] To identify the network(s) controlled by *SLNCR*, we overexpressed *SLNCR* in A375 melanoma cells and performed bulk RNA sequencing (RNA-seq) and differential expression analysis between empty vector control (empty) and *SLNCR*-overexpressing (*SLNCR*) cells (Table S1, tab 1). We then searched for TF binding sites (TFBSs) among the promoters and promoter-proximal regions of differentially expressed genes using TF footprinting data from the Encyclopedia of DNA Elements (ENCODE) (Table S1, tab 2). The Fisher exact test identified BSs for the TFs SMARCA4, E2F1, and FOSL2 in 61%, 9.7%, and 2.7%, respectively, of the differentially expressed genes affected (Figure 1A; Table S1, tab 3). This analysis implies that genes containing the E2F1 DNA binding element are affected by *SLNCR* expression.

We also examined target gene expression levels as a function of *SLNCR* and TF levels using data from TCGA (accessed 2019). This analysis, named ‘‘disease-associated transcriptional network analysis’’ (DATNA; see STAR Methods), identifies TF-target gene correlations as

a function of *SLNCR* levels across large, patient-derived datasets, which maintains clinical significance compared to cell line data. We examined skin cutaneous melanoma (SKCM) samples and identified 161 *SLNCR*-E2F1, 32 *SLNCR*-TEAD1, 24 *SLNCR*-LTBP3, 19 *SLNCR*-TCF3, and 25 *SLNCR*-SREBF2 gene dependency ‘‘triads’’ (Figure 1B).

Next, we used the cancer dependency map portal DepMAP (https://depmap.org/portal/) to functionally examine the interconnectivity between the TF-target gene triads in melanoma cell growth. Through DepMAP analysis, we identified 32 genes from the 161 *SLNCR*-E2F1 triads as melanoma gene dependencies (Table S1, tab 4). By comparison, 7 genes were identified as *SLNCR*-LTBP3, 6 as *SLNCR*-SREBF2, and 4 each as *SLNCR*-TCF3 and *SLNCR*-TEAD1 melanoma dependencies.

Finally, we cross-validated the gene triads identified by DATNA and DepMAP with our RNA-seq data. Ten of the *SLNCR*-E2F1 triads were differentially expressed upon *SLNCR* overexpression in A375 cells and 2 each of the *SLNCR*-LTBP3, *SLNCR*-TCF3, and *SLNCR*-SREBF2 triads. No differentially expressed *SLNCR*-TEAD1 triads were identified. By combining multiple analyses of large clinical and experimental datasets, we identified E2F1, SREBF2, TEAD1, TCF3, and LTBP3 as potential oncogenic partners of *SLNCR* in melanoma.

SLNCR-E2F1 demonstrated the greatest number of coordinately regulated genes, functional dependencies, and melanoma dependencies. Moreover, we had previously demonstrated that E2F1 interacts with *SLNCR* using RNA-associated TF array (RATA),[12] a result that we further validated by immunoprecipitation of endogenous E2F1 followed by qPCR quantification of *SLNCR* in HEK293T cells (Figures S1A and S1B). Thus, we decided to characterize the *SLNCR*-E2F1 interaction and its function in melanoma in detail.

To assess the combined effect of *SLNCR* and E2F1 on outcomes of patients with melanoma, we interrogated melanoma TCGA RNA-seq datasets for patient survival stratified by (1) high *SLNCR* and high *E2F1*, (2) high *SLNCR* and low E2F1, (3) low *SLNCR* and high *E2F1*, and (4) low *SLNCR* and low *E2F1* levels (Figure 1C). Kaplan-Meier analysis revealed that patients with high *SLNCR* and high E2F1 levels had worse overall survival (OS) (median $OS^{HS/HE}$ = 431 days, $p = 0.015$) compared to the expected control (median $OS^{Ctrl\text{-}HS/LE}$ = 777 days). Patients with high *SLNCR* and low E2F1 did not deviate significantly from the respective control (median $OS^{HS/LE}$ = 719 days and median $OS^{Ctrl\text{-}HS/LE}$ = 777 days, $p = 0.83$). The same was observed for patients with low *SLNCR* regardless of E2F1 levels (median $OS^{LS/HE}$ = 730 days and $OS^{Ctrl\text{-}LS/HE}$ = 733 days, $p = 0.91$, for the high-E2F1 group and median $OS^{LS/LE}$ = 724 days and median $OS^{Ctrl\text{-}LS/LE}$ = 731 days, $p = 0.096$, for the low-E2F1 group). That is, high levels of either *SLNCR* or E2F1 in isolation did not affect patient survival. When both are overexpressed, *SLNCR* and E2F1 negatively affect patient outcomes. These analyses support the hypothesis that *SLNCR* and E2F1 coordinately regulate genes with functions in melanoma and that the adverse effects of *SLNCR* on patient survival depend on its cooperative activity with E2F1.

To explore this hypothesis, we overexpressed *SLNCR* in A375 melanoma cells with and without E2F1 depletion and measured proliferation and invasion. A375 cells express

relatively low levels of *SLNCR* as compared to patient-derived melanoma short-term cultures (MSTCs)[11] and high endogenous levels of E2F1.[10] *SLNCR* overexpression (Figure S1C) increased A375 cell invasion and proliferation compared to empty vector control by a minimum of ~1.5-fold (Figures 1D and 1E). Silencing E2F1 (Figures S1C-S1E) reduced cell invasion by ~13% compared to scramble control (Figure 1D) and proliferation by 3.5-fold (Figure 1E). E2F1 knockdown in the *SLNCR* overexpression background (Figures S1C-S1E) reversed the effect of *SLNCR* overexpression on A375 cell invasion by ~30% (Figure 1D) and proliferation by ~10-fold (Figure 1E). We also performed E2F1 depletion in WM1575 and WM1976 (Figures S1C-S1E) and assessed the ability of E2F1-depleted cells to invade (Figure 1F) and proliferate (Figure 1G). Even with high *SLNCR* expression in the MSTCs, depletion of E2F1 was detrimental to melanoma progression. These experiments support the conclusion that *SLNCR* and E2F1 coordinately regulate melanoma-relevant pathways.

E2F1 binds to the RNA analog of the cognate E2F1 BS on DNA

To identify *SLNCR*-interacting proteins, we performed a proteome-wide yeast three-hybrid (Y3H) screen[17,18] (Figure S2A). Four of the candidates predicted by DATNA (E2F1, TEAD1, TCF3, and SREBF2) were hits in this assay (Figure S2B). Notably, E2F1 was previously reported to interact with *SLNCR*.[11,12,14] To identify the RNA sequences within *SLNCR* that bind to E2F1, we performed pairwise Y3H screens of nine partially overlapping 300-nt-long segments of *SLNCR* against E2F1 (Figure 2A). Yeast expressing *SLNCR* segments 2 and 3 grew on selective media, suggesting complex formation (Figure S2C). By analyzing the sequence of *SLNCR*, we identified 5 regions within segments 2 and 3, with analogy to the cognate E2F1 DNA-binding motif (5′-TTTC[CG]CGC-3′; Figures 2A and 2B). We named those sequences binding sites 1–5 (BS1–5).

To assess E2F1 binding to each one of the BSs, we performed RNA electrophoretic mobility shift assays (REMSAs) using purified, full-length E2F1 and 3′-biotin-labeled *SLNCR* RNA oligos. Secondary structure predictions of each BS in isolation[19,20] indicated that they could adopt single-strand (loop), double-strand (stem), or mixed (hybrid) secondary structures. We tested probes containing each putative BS in loop, stem, or hybrid contexts by REMSA. We detected E2F1 binding to loops and stems but not to hybrid probes (Figure 2C). Notably, probing of *SLNCR* by dimethyl sulfate and mutational profiling (DMS-MaP)[21] in A375 cells (Figures 2B, S2D, and S2E) showed that BS1–5 of intracellular, full-length *SLNCR* had low DMS reactivities, consistent with double-strand structures, suggesting that all BSs could interact with E2F1 in cells.

We next incubated 0.5 μM of purified E2F1 with increasing concentrations of double-strand BS1–5 and quantified the signal of E2F1-bound over unbound RNA (Figure S2F). By comparing the concentrations of RNA required for electromobility shift, we assessed the relative affinity of E2F1 for either of the BSs on *SLNCR*. BS3 bound to E2F1 with higher affinity than the other BSs because a shifted band could be detected with as little as 12.5 nM of RNA. The other BSs required at least 50 nM for a shifted band to appear (Figure S2F).

BS1–2-3 and BS4–5 are contained in two relatively short sequence segments of *SLNCR* (nucleotides 186–251 and 608–659, respectively) (Figure S2D). We hypothesized that two

of the BSs within full-length, intracellular *SLNCR* may mediate E2F1 binding together. We assessed relative E2F1 binding affinity for *SLNCR* fragments containing two proximal BSs using 60-mer RNA oligonucleotides containing BS1+2, BS2+3, and BS4+5 (Figures 2D and S2F). Electrophoretic mobility shift was detected with as little as 12.5 nM of either of the combination BSs. Moreover, the shifted bands at 12.5 nM of labeled RNA were more intense for the BS1+2 and BS2+3 oligonucleotides compared to BS4+5 or BS3 alone, suggesting that BS1+BS2 and BS2+BS3 can act cooperatively to bind E2F1 with higher affinity compared to other oligonucleotides. Because BS2+3 gave the best apparent affinity for E2F1, we incubated increasing amounts of recombinant E2F1 to saturating concentrations of labeled BS2+3 (Figure S2F). We observed that 100 nM of BS2 +3 bound to 0.085 μM of E2F1, confirming a higher affinity of E2F1 for BS2+3 (Figure S2F).

We hypothesized that the secondary structures of the oligonucleotides used for REMSA influenced the electrophoretic mobility properties of their complexes with E2F1. We, therefore, performed secondary structure predictions of the oligonucleotides used for REMSA. BS1+2 and BS2+3 were predicted to form mostly double-strand structures (data not shown; Figure S2G). BS3 is almost perfectly complementary to BS2 (Figure 2B), and thus, the BS2+3 oligonucleotide formed a perfect double-strand structure (Figure S2G). Double-stranded oligonucleotides bound with higher relative affinities to E2F1, suggesting that these RNAs might mimic DNA binding to E2F1.

SLNCR-E2F1 complex formation promotes melanoma invasion and proliferation

We previously showed that *SLNCR* overexpression increased A375 melanoma invasion by 1.6-fold and proliferation by ~1.5-fold compared to controls (Figures 1D and 1E). To test whether E2F1 mediates these *SLNCR*-dependent effects, we transfected inhibitory oligonucleotides corresponding to E2F1 BS2+3 of *SLNCR* (RNA mimic 2+3) into *SLNCR*-overexpressing A375 cells and MSTCs. Consistent with *SLNCR*-E2F1 complexes coordinately regulating melanoma processes, RNA mimic 2+3 reduced invasion and proliferation by a minimum of 2-fold each, as compared to respective controls (Figures 3A and 3B).

To assess the roles of the *SLNCR*-E2F1 complex in melanoma *in vivo*, we generated a mouse model of metastatic melanoma by injecting NSG mice with A375-Luc2 cells overexpressing *SLNCR* that had been incubated with either RNA mimic 2+3 or a control oligonucleotide (Figures 3C and 3D). A375-Luc2 cells express luciferase, which produces bioluminescence upon the breakdown of its substrate. In this model, bioluminescence is a proxy for melanoma proliferation and migration of melanoma cells from the bloodstream into the lungs (extravasation), a common site of melanoma metastasis.[22] We observed a significant reduction in luminescence in the lungs of the mice injected with cells treated with RNA mimic 2+3 compared to control (Figures 3C, 3D, and S3D). Importantly, RNA mimic 2+3 blocked the *SLNCR*-E2F1 interaction (Figure S3A) and reduced melanoma invasion and proliferation *in vitro* and extravasation *in vivo* without affecting the levels of the E2F1 protein or *SLNCR* transcript (Figures S3B and S3C).

These data demonstrate that the *SLNCR*-E2F1 complex mediates melanoma proliferation and invasion and that blocking their interaction can slow melanoma pathogenesis. Because

E2F1 regulates numerous fundamental biological processes,[2] selectively blocking the *SLNCR*-E2F1 interaction could provide a novel therapeutic modality without the global effects of inhibiting all E2F1 activities.

E2F1 binds RNA via its DNA binding domain

We hypothesized that RNA and DNA compete for the same BS on E2F1 because the E2F1 BSs within *SLNCR* are analogous to the cognate E2F1 DNA-binding motif (Figure 2B) and because BS2+3 can form dsRNA (Figure S2G). To test this hypothesis, we performed RNA/DNA competition assays for E2F1 binding.[23] EMSA with full-length E2F1, biotin-labeled DNA, and increasing amounts of unlabeled RNA showed that as little as 50 nM RNA competed with 100 nM DNA (Figure 4A), showing that RNA binding and DNA binding were mutually exclusive. Conversely, 30 μM of unlabeled DNA was unable to completely compete with 50 nM biotin-labeled RNA (Figure 4A).

To test whether RNA can bind to E2F1^{DBD}, we repeated these experiments using purified recombinant E2F1^{DBD} (residues 110–194) (Figure S3E). We found that 250 nM of RNA almost completely displaced bound DNA (~15% of E2F1-bound DNA left) compared to the 40 μM of DNA required to displace 50 nM of RNA (~19% of E2F1-bound RNA left) (Figure 4B). Hence, RNA and DNA compete for binding to E2F1^{DBD}. Because of the reverse complementarity of BS2 and BS3, the RNA oligo BS2+3 forms a hairpin structure involving the E2F1 BSs. We performed all experiments at 37°C and pH 7.3, which, in theory, should maintain the folded conformation. Likewise, all dsDNA used in competition assays had been pre-annealed, ensuring that no single-stranded DNA was present in the reaction mixes. We performed competition assays with labeled RNA or DNA. We did not see a reduction in signal upon the addition of increasing amounts of DNA to labeled RNA. However, very low concentrations of unlabeled RNA reduced the signal corresponding to labeled DNA. If E2F1 bound RNA-DNA hybrids, we would see similar signal intensities for both competition assays irrespective of which nucleic acid was labeled. Thus, it is not likely that E2F1 bound to RNA-DNA hybrids in competition assays.

We next used MD simulations to define the contacts between nucleic acids and E2F1. Because Å-resolution structures of nucleic-acid-bound E2F1 are not available, we generated an *in silico* model using AlphaFold2[24] and homology modeling. This model was highly similar to the crystal structure of the closely related E2F4^{DBD},[25] with a root-mean-square deviation (RMSD) of 0.73 Å. Furthermore, using a 15-mer reference dsDNA containing the consensus E2F1-binding element, we showed that the solvated E2F1^{DBD} had low-level RMSDs and root-mean-square fluctuations (RMSFs) at the DNA-binding residues in the absence of DNA, which were further reduced in the presence of DNA (Figures S4A-S4D). We observed a high degree of stability throughout E2F1^{DBD} except for the 10 C-terminal residues, which were not involved in nucleotide binding. Together, these observations suggested that our model was suitable for studying the structural and dynamic properties of E2F1^{DBD} bound to DNA (Table 1 and Table 2).

We modeled DNA binding either using the reference 15-mer dsDNA containing the consensus motif[26] (Videos S1 and S5; Figures S4A-S4D) or the previously described 42-mer dsDNA (Videos S2, S6A, and S6B) shown to bind to recombinant E2F1 by EMSA (Figures

S4E-S4H). RNA binding was modeled using the 60-mer *SLNCR* fragment containing BS2+3 (60-mer BS2+3 RNA; Videos S3 and S7) that bound to E2F1 in REMSA (Figures S4I and S4J). Initial MD simulations showed that the binding of both the 42-mer dsDNA and the 60-mer BS2+3 RNA reduced the observed RMSD or RMSF of free $E2F1^{DBD}$ (Figures S4E-S4J) without affecting its structural features (Videos S6A, S6B, and S7). These results suggested the formation of stable, biologically relevant complexes. The 60-mer BS2+3 RNA folded into a straight double-helical segment resembling dsDNA but showing a higher degree of mobility (backbone RMSD = 15.7 A; Figure 4C; Videos S3 and S7). The 15- and 42-mer dsDNA formed straight double helices within the $E2F1^{DBD}$ interacting region and did not show a high degree of mobility (backbone RMSDs = 2.5 and 5.2 A, respectively; Figure 4D; Videos S5, S6A, and S6B).

Repeating the simulations with a 60-mer *SLNCR* fragment containing BS1+2 (60-mer BS1+2 RNA) showed that this fragment formed a “curved” structure, suggesting that this conformation limited E2F1 binding (Video S4). This observation was consistent with the lower apparent affinity of the BS1+2 oligo in REMSA (Figures 2D and S2F). We conclude that the more “linear” structure of the 60-mer BS2+3 RNA was important for binding to $E2F1^{DBD}$, as it likely mimics linear DNA.

Next, we compared the MD models of $E2F1^{DBD}$+60-mer BS2+3 RNA and $E2F1^{DBD}$+15-mer dsDNA. We calculated the relative interaction strengths for each $E2F1^{DBD}$ residue forming contacts with nucleotides (Figure 4E). To do this, we averaged the predicted interaction energy of each amino acid-nucleotide pair in the complexes between $E2F1^{DBD}$ and the 15-mer reference dsDNA, the 42-mer dsDNA, or the 60-mer BS2+3 RNA over the total number of MD runs for each complex. We then defined a threshold (−9.8 kcal/mol) to segregate strong from weak interactions. The −9.8 kcal/mol threshold was empirically determined based on the overall interaction energy average observed across all residues of the $E2F1^{DBD}$+15-mer reference dsDNA model. Residues with average predicted interaction energies lower than −9.8 kcal/mol were defined as strong interactors, and those higher than −9.8 kcal/mol were considered weak interactors.

We identified three key regions that contact RNA and DNA nucleotides alike: Lys120, Lys125, and Arg127 in region 1; Arg165, Arg166, and Tyr168 in region 2; and Lys182 and Lys185 in region 3 (Figure 4E). Although most contacts contributed similarly to DNA and RNA binding, we note that Lys125 and Arg127 contributed more to DNA as compared to RNA binding (−12.5 compared to −5.2 kcal/mol and −31.2 compared to −13 kcal/mol, respectively; Figure 4E) because they made strong salt bridge contacts with the phosphate backbone of DNA. In contrast, other amino acids of $E2F1^{DBD}$ contributed exclusively to RNA binding: Pro122, Gly123, and Glu124 in region 1; Lys161 and Val162 in region 2; and Lys183 and Ser184 in region 3. Adding all interaction strengths together suggested that E2F1 binds to DNA with ~25 kcal/mol higher affinity than to RNA (Figure 4F) and that E2F1-DNA complex formation is thermodynamically more stable than E2F1-RNA complex formation. This result contrasts with the competition experiments, which showed that E2F1 bound to RNA with higher relative affinity than to DNA (Figures 4A and 4B).

Most E2F1^{DBD} residues that contribute to DNA binding also contribute to RNA binding

Having compared relative DNA and RNA binding affinities, we assessed relative E2F1 binding specificities. TFs recognize specific DNA sequence motifs, and their sequence specificity is determined by amino acid-nucleobase contacts. We classified all residue contacts from our MD models with base, phosphate, or sugar moieties (Figures 5 and S5).

1. The reference 15-mer dsDNA had 66 base contacts, 46 phosphate contacts, and 47 sugar contacts (Figures 5A and 5D). E2F1 formed base contacts, mainly with nucleotide segments C5–G8 and T14-T15 in one strand and A30–A27 and C21–A19 in the complementary strand. The E2F1 consensus spans nucleotides T2–C9 and their complementary pairs A30–G22. The greatest numbers of base contacts were with nucleotides G6 (9 contacts), G20 (14 contacts), and A29 (13 contacts), suggesting that these three nucleotides play a major role in E2F1 sequence-specific DNA binding. Nucleotides T4, G8, T15, A19, C21, and A28 had fewer base contacts (between 1 and 5), suggesting minor roles in sequence specificity.

2. There are two copies of the E2F1 consensus binding motif on the 42-mer dsDNA (Figures 5B and 5D). The 5′ motif spans nucleotides T6–G13 and the 3′ motif spans nucleotides C56–T49 in the antisense direction. We found 59 base contacts, 48 phosphate contacts, and 47 sugar contacts with the 5′ motif and 60 base contacts, 48 phosphate contacts, and 50 sugar contacts with the 3′ motif. All contacts with the 5′ motif were within nucleotide segments T8–T20 in the first strand and A80–T68 in the complementary strand. All contacts with the 3′ motif were within the nucleotide segments A26–T39 in the first strand and T63–T50 in the complementary strand.

3. The 60-mer *SLNCR* RNA had 47 base contacts, 38, phosphate contacts, and 46 sugar contacts (Figures 5C and 5D). BS2 spans nucleotides U8–G14 in a 5′ to 3′ orientation, and BS3 runs in the 3′ to 5′ direction and spans nucleotides G45–A52. Unlike the MD models containing DNA, which only formed protein-nucleic acid contacts locally at and immediately surrounding the E2F1 binding motif (Figures 5A and 5B), the interactions with RNA appeared to spread across the double-strand length of the 60-mer BS2+3 RNA (Figure 5C). Based on this observation we hypothesized that RNA “bends” to contact E2F1 at residues beyond the nucleic acid binding pocket (Figure 4C).

To test this hypothesis, we plotted the base, phosphate, and sugar interactions per amino acid across E2F1^{DBD} (Figures S5A-S5C). This analysis revealed that the same amino acids were involved in nucleic acid interactions with DNA and RNA. However, several additional residues that did not contact DNA did form contacts with RNA. Specifically, E175, G176, and Q178 mostly contacted the nucleobase, and K183-S184 made a similar number of contacts with base, sugar, and phosphates. These data indicate that many of the contacts that mediate specific DNA also mediate RNA binding. However, there are additional nucleobase contacts that contribute to RNA binding.

These data demonstrate several key points: the overall length of the nucleic acids did not contribute to specificity or affinity, as binding was mostly confined to the E2F1 binding motif. Binding to phosphates increased complex stability, as these contacts created strong salt bridges, which explains the higher relative thermodynamic stability of the E2F1^{DBD}+DNA complexes as compared to the E2F1^{DBD}+RNA complex. The greater number of base contacts within and immediately surrounding the E2F1 consensus sequence in the E2F1^{DBD}+RNA model (22 vs. 15 in the E2F1^{DBD}+dsDNA 42-mer model) suggests that multiple RNA conformations might contribute to E2F1 binding specificity. Taken together, these observations suggest that the extended contacts observed for RNA in the E2F1^{DBD}+60-mer BS2+3 RNA MD model are likely transient. We speculate that the 60-mer BS2+3 RNA assumes multiple conformations within E2F1^{DBD} and can, thus, displace the 42-mer dsDNA in our competition assays despite having a lower apparent relative affinity.

A disease-associated mutation in the E2F1 DNA binding domain maintains RNA binding

Two reported E2F1^{DBD} mutations (R166H[27] and L132E[28]) disrupt DNA binding. R166H is a naturally occurring somatic mutation found in patients with mesothelioma that reduces E2F1 gene promoter occupancy, as shown by chromatin immunoprecipitation (ChIP).[27] L132E is an engineered mutation that reduces E2F1 occupancy at E2F1 and CDC6 promoters.[28,29] However, the effects of these mutations on E2F1 binding to DNA were not tested directly *in vitro*. For the R166H mutation, we only considered the neutral form of His166.

We performed EMSA and MD simulations to assess the effect of these mutations on nucleic acid binding (Figures 6 and S6). Surprisingly, neither mutant affected 42-mer dsDNA or 60-mer BS2+3 RNA binding in our EMSA experiments (Figure 6A). Similarly, we did not detect differences in the stabilities of L132E or R166H mutant E2F1^{DBD} alone or in complex with 15-mer reference dsDNA, as shown by low RMSDs and RMSFs that would affect DNA binding in MD simulations (Figure S6). Finally, calculating the average residue interaction energies of E2F1 mutants using molecular mechanics/generalized Born surface area (MMGBSA) showed that neither mutation compromised nucleic acid binding (Figures 4F, 6B, and 6C). Notably, the L132E mutation did not significantly contribute to binding energies (Figure 4E), and thus, it is not surprising that this mutation did not affect nucleic acid binding. Even though Arg166 is one of the major contributors to thermodynamic energy in all MD models, it is only 1 of 20 (in 42-mer dsDNA) and 1 of 19 (in 60-mer BS2+3 RNA) residues that contact the nucleic acid, possibly explaining why this mutation did not affect binding to either nucleic acids (Figures S5A-S5C).

E2F1 binding to RNA precludes DP1 binding

DP1 binds to the same DNA sequence as E2F1.[25] Unlike with DNA binding, DP1 did not enhance E2F1 binding to the 60-mer BS2+3 RNA in REMSA experiments (Figure 7A). In our E2F1^{DBD}-DP1^{DBD}+15-mer dsDNA model (Figure 7B; Video S8), E2F1 maintained minimum contacts with DP1. Most DP1-E2F1 interactions were hydrophobic, and there was only one salt bridge between Glu175 of E2F1 and Arg117 of DP1 at the E2F1-DP1 interface. The RMSDs and RMSFs of E2F1^{DBD} remained minimal in this model (Figures S7A and S7B). However, DP1 exhibited a high degree of RMSFs at a flexible loop not in

contact with E2F1 or the DNA (residues Glu145–Ile165; Figure S7C). In addition, the DNA was rigid when E2F1 bound (RMSD = 3.2 A). These observations suggested that $E2F1^{DBD}$ and $DP1^{DBD}$ do not associate in the absence of DNA. In contrast, the 60-mer BS2+3 RNA could not simultaneously bind to E2F1 and DP1 due to steric clashes from the 60-mer RNA in the region where DP1 interacts with E2F1 in the E2F1-DP1 complex (simulation was not possible), corroborating the result of our REMSA (Figure 7A).

To model the interaction of $E2F1^{DBD}$-$DP1^{DBD}$ with RNA, we generated a 15-mer, B-form dsRNA by directly converting the 15-mer dsDNA into 15-mer dsRNA (Figure S7D; Video S9) and ran MD simulations. Like the $E2F1^{DBD}$-$DP1^{DBD}$+15-mer dsDNA model, the RMSDs and RMSFs of $E2F1^{DBD}$ remained minimal in the model with 15-mer dsRNA (Figures S7E and S7F), and DP1 exhibited a high degree of RMSFs at the flexible loop (Figure S7G). The 15-mer dsRNA was very flexible (RMSD ≅ 13 Å; Figure S7D), suggesting that the $E2F1^{DBD}$-$DP1^{DBD}$+15-mer dsRNA is less stable than the $E2F1^{DBD}$-$DP1^{DBD}$+15-mer dsDNA complex.

$E2F1^{DBD}$ and $DP1^{DBD}$ both carry net positive charges (+4 and +6, respectively), which play key roles in interactions with the negatively charged phosphate backbones of nucleic acids. The 15-mer dsDNA has a net negative charge (−30) that counterbalances the net positive charges of the proteins. $E2F1^{DBD}$ made contacts with the 15-mer dsDNA on the E2F1 BS or on the nucleotides directly surrounding it. $DP1^{DBD}$ formed extensive contacts across the 15-mer dsDNA (Figure 7E). Plotting the base, phosphate, and sugar interactions per amino acid across $E2F1^{DBD}$ revealed that adding $DP1^{DBD}$ to the system did not alter the contact pattern compared to $E2F1^{DBD}$ alone (Figure S5D). Taking these results together, this model supports that E2F1 guides target specificity and DP1 secures the complex by increasing its affinity for DNA. Similarly, the 15-mer dsRNA bound to both E2F1 and DP1 and stabilized a ternary complex (Figure 7F). All oligonucleotides used in the study have been listed in Table 2 in STAR Methods.

DISCUSSION

TFs recognize specific DNA sequences to activate or repress target gene transcription. Increasing numbers of TFs are found to bind RNA, establishing dual nucleotide binding activities.[30-41] To the best of our knowledge, this is the first example of a TF with RNA- rather than DNA-dependent oncogenic activity.

Oncogenic roles have been previously ascribed to proteins and lncRNAs that can form complexes (e.g., polycomb repressive complex 2 [PRC2] and the lncRNAs *HOTAIR* and *XIST*).[42-50] In these examples, both PRC2 and the lncRNAs are oncogenic independently of the lncRNA-PRC2 interaction. By association, the oncogenic effects of these lncRNAs have been ascribed to the PRC2-lncRNA interaction. Here, we show that the oncogenic activity requires *SLNCR*-E2F1 complex formation and that overexpression of either molecule without complex formation had no effect.

Recently, Oksuz et al. showed that half of the TFs expressed in K562 cells, including E2F3, E2F4, and E2F6, can bind RNA[51] mostly through ARM domains. The ARM domain in

these TFs is adjacent to their DBD, and RNA binding does not preclude DNA binding. E2F1 does not contain an ARM domain, but it has a di-RG repeat, which is predicted to mediate RNA binding[15] adjacent to its DBD. Here, we showed that $E2F1^{DBD}$ alone bound RNA, as our $E2F1^{DBD}$ construct did not include the di-RG motif.

We showed that RNA outcompeted DNA for binding to limiting amounts of E2F1. MD simulations demonstrated that dsDNA was rigid and bound tightly to $E2F1^{DBD}$ at Lys125 and Arg127. However, BS2+3 RNA was more flexible and made more amino acid contacts with $E2F1^{DBD}$ than DNA. Thus, E2F1-DNA binding may be more thermodynamically favorable, akin to a “lock and key” interaction, while E2F1-RNA binding may be more kinetically favorable, akin to an “induced fit” interaction.

We speculate that RNA competes with DNA and DP1 for binding to E2F1. In cases of pre-existing E2F1-DP1 dimers, DNA binding might be favored (Figure 7). Once E2F1 and DP1 dissociate from DNA and each other, E2F1-RNA binding might be favored, as the RNA binds E2F1 faster and more extensively than DNA. This effect may be enhanced by the presence of multiple E2F1 BSs within *SLNCR*, such that one *SLNCR* molecule might interact with multiple E2F1 molecules. Thus, one *SLNCR* transcript might recruit multiple E2F1 molecules to a given promoter independently of DP1.[3] These observations set the stage for broadening the regulatory network of TFs by interactions with lncRNAs.

R166H and L132E mutants were previously reported to reduce the DNA binding activity of E2F1. MD simulations predicted that these mutations only slightly reduced E2F1 binding energy to nucleic acids. Consistent with these simulations, we did not detect an apparent reduction in $E2F1^{DBD}$ binding affinity to RNA or DNA by REMSA (Figure 6A). These mutations reside in the helix-loop-helix region of E2F1, which is not essential for DNA binding, whereas residues 117–128 reside in the basic region which is essential for DNA binding *in vitro*.[52]

Our data are consistent with a model in which *SLNCR* binds to E2F1 to drive melanoma progression, independent of E2F1 DNA binding. More invasive melanomas are less proliferative, and vice versa, more proliferative melanomas are less invasive.[53] E2F1 regulates both processes.[2] It is, therefore, possible that *SLNCR* toggles E2F1 activities between proliferation and invasion. It is easy to envision that *SLNCR*-E2F1 complexes activate the transcription of certain melanoma-relevant genes while preventing E2F1 binding to and recruitment of DP1-E2F1 to other melanoma-relevant promoters, thereby shifting melanomas between proliferative and invasive stages of oncogenesis.

Concordant with our results, a randomized library screen of synthetic RNA oligos for competition with DNA for E2F1 binding[54] showed that RNA could prevent E2F1 from binding to DNA *in vitro* and that a short RNA oligonucleotide efficiently inhibited cell proliferation. Administering oligonucleotides that block *SLNCR*-E2F1 complex formation significantly reduced lung extravasation, suggesting that this complex is a promising therapeutic target.

Limitations of the study

We demonstrate that the *SLNCR*-E2F1 interaction drives melanoma progression and that inhibiting this interaction without reducing the levels of either molecule prevents melanoma extravasation into the lungs. We did not model other stages of melanoma progression. Using $E2F1^{DBD}$ allowed us to better control the MD simulation parameters; however, we acknowledge that the overall conformation of E2F1 and its binding interactions may change in the context of the whole protein. Additionally, we showed that RNA bound to $E2F1^{DBD}$ better than the corresponding DNA element. E2F1 typically binds to DNA as a heterodimer with DP1. We could not assess the role of the E2F1-DP1 interaction on relative RNA or DNA binding. Protein binding can affect the lncRNA secondary structure. Thus, the binding of other proteins to *SLNCR* might affect the local structure at the E2F1 BS to modulate its ability to phenocopy the E2F1 DNA binding element. Finally, as more samples of patients with melanoma become available, we may gain greater insights into how the *SLNCR*-E2F1 interaction affects melanoma progression and patient survival.

STAR★METHODS

EXPERIMENTAL MODEL AND STUDY PARTICIPANT DETAILS

Four-week-old female NSG mice (NOD.Cg-Prkdcscid Il2rgtm1Wjl/SzJ, The Jackson Laboratory, #005557) were used in the animal experiments. Ethical approval was obtained from Dana-Farber Institutional Animal Care and Use Committee (IACUC) approved protocol #23-001. A375-Luc2 cell lines used for the lung extravasation mouse model was obtained from ATCC (ATCC, CRL-1619-LUC2) and was validated by ATCC using STR profiling and tested negative for mycoplasma contamination at DFCI Animal Resources Facility.

Sex differences do exist in melanoma outcomes with females having better prognosis than males.[70] However, the reasons for the female-favoring bias are poorly understood. A375 is derived from a female-derived melanoma and these cells were transferred into female NSG mice. These mouse experiments directly assessed melanoma extravasation from the bloodstream to the lungs over 7 days. This process is not known to be affected by sex differences. Moreover, *SLNCR* and E2F1 protein levels are not known to be different between the sexes. If anything, any processes affected in female models of melanoma would be expected to be worse in male mice and/or using male-derived melanomas. Thus, the results described here can be extrapolated to male mice.

METHOD DETAILS

Cell culture: A375 (ATCC, CRL-1619) and HEK293T cells were a gift from Ronny Drapkin. A375 and HEK293T cells were cultured as adherent cells in Dulbecco's modified eagle medium (DMEM, Invitrogen) supplemented with 10% fetal bovine serum (FBS). WM1575 and WM1976 are patient derived melanoma short-term cultures (MSTCs) from collections of the Wistar Institute.

Stable A375 cells overexpressing *SLNCR* were generated by transfecting cells with pcDNA3.1 plasmid consisting of puromycin resistant gene and CAG promoter. After 48 h of

growth in complete DMEM media containing 2 μg/mL puromycin, single cells were sorted into a 96-well plate. Individual clones were picked and used for all downstream experiments.

For proliferation assays, stable cells or MSTCs were seeded at 0.01x10 cells/well in a 24-well plate 48 h after infection with lentiviral particles containing E2F1 shRNAs or 48hrs after transfection with 1 μM RNA Mimic 2 + 3 oligo and proliferation was measured every 48 h by manual cell counting using hemocytometer and trypan blue dye.

For migration and invasion assays stable A375 cells or MSTCs were infected with lentiviral particles containing E2F1-knock down shRNA or transfected with the RNA Mimic 2 + 3 oligo 48 h post-seeding. 2.5x10 A375 cells or 0.1x10 WM1976 or 7.5x10 WM1575 cells in serum-free media were plated in either BD BioCoat matrigel inserts or uncoated control inserts (Corning), placed into DMEM with 30% FBS, and incubated for 16 h. Cells that did not migrate or invade were removed using a cotton tipped swab, chambers were rinsed twice with PBS, and stained using Fisher HealthCare PROTOCOL Hema 3 Fixative and Solutions. Cells were imaged on 20x magnification in 3 fields of view for 3 technical replicates for each of the 3 independent biological replicate experiments.

$$\%\ Invading\ cells = \frac{Mean\ number\ of\ cell\ invading\ through\ Matrigel\ insert}{Mean\ number\ of\ cells\ invading\ through\ control\ insert} \times 100$$

Lipofectamine 2000 (Life Technologies, 11668027) was used for all plasmid transfections following the manufacturer's protocol.

Plasmid construction: *SLNCR* fragment was synthesized by Biomatik Corporation. Cloning for E2F1 shRNA into plko plasmids was done as previously described in Addgene Plasmid 10878 Protocol Version 1.0. December 2006.

Protein production plasmids were created by introducing synthetic gene fragments containing wildtype, L132E and R166H mutant $E2F1^{DBD}$ (residues 110–194) with an N-terminal His6-tag followed by a TEV protease cleavage site into pET28a SpyCatcherSnoopCatcher (gifted from Mark Howarth, Addgene plasmid #72324) by Gibson assembly. Gene fragments were synthesized by IDT. Fragments were extended by PCR with primers E2F1-DBD-f and E2F1-DBD-r (See Table 2) to introduce overlapping handles for Gibson Assembly and to introduce a C-terminal stop codon. After transformation in chemocompetent 5-α cells (NEB, C2987H), plasmids were isolated and verified by Sanger sequencing. For protein production verified plasmids were transformed into chemocompetent BL21(DE3) pLysS cells (Invitrogen, C606010). $E2F1^{DBD}$(110–194): MGSS**HHHHHH**SSG*ENLYFQ*GRGRHPG KGVKSPGEKSRYETS**L**NLTTKRFLELLSHSADGVVDLNWAAEVLKVQKR**R**IYDITN VLEGIQLIAKKSKNHIQWLGSH. His-tag is bolded, TEV cleavage site is italicized and $E2F1^{DBD}$ residues immediately follow TEV cleavage site, and residues Leu132 and Arg166 are bolded.

For yeast-three-hybrid, full length *SLNCR* or *SLNCR* fragments were ordered as gblocks from IDT and digested with SphI-HF (NEB, R3182S) and SmaI (NEB, R0141S) restriction

enzymes in CutSmart buffer (NEB, B6004S). *SLNCR* fragment 1 was digested using SphI-HF only. Digestion was then purified using PCR purification kit (Qiagen). Purified DNA was then ligated into SphI/SmaI digested pIIIA-MS2–1 (gift from Marvin Wickens, Addgene plasmid #220631) plasmid using T4 DNA ligase (NEB, M0202S) and transformed into chemocompetent 5-α cells (NEB, C2987H).

Yeast three hybrid (Y3H): These experiments were conducted according to established protocols[55] with the following modifications for ORFeome-wide screening. *SLNCR* full length and *SLNCR* fragments-expressing plasmids (harboring Uracil auxotrophic marker), using standard protocols. Transformed yeast were selected by spotting on SC plates depleted of uracil (SC-U). Protein-expressing (pools of 100 strains) plasmid collection (DFCI-hORF8.1 collection gifted by Marc Vidal, Center for Cancer Systems Biology at Dana-Farber Cancer Institute) harboring Tryptophan auxotrophic marker, was contained into the yeast strain Y8800 and grown in SC-plates depleted of tryptophan (SC-W). Yeast strains YLW3α containing the examined *SLNCR* fragment plasmids were mated with the Y8800 yeast strains containing the protein plasmids. Mating was performed in YPD media overnight, and diploids carrying both plasmids were selected in liquid SC media depleted of tryptophan and uracil (SC-WU) for 1 day. Double selected yeast was then plated on solid agar in the absence of HIS (SC-WUH) and different concentrations 3AT, a competitive inhibitor of the HIS3 gene product, to increase the stringency of the selection. Colony growth was assessed after 5 days of growth and identity of the interacting pairs was confirmed by Sanger sequencing. For pairwise screen, same approach was used, but only selected proteins plasmids from the DFCI-hORF8.1 collection were transformed into yeast to test the specific binding of that protein with full length *SLNCR* or E2F1 with *SLNCR* fragments. The 3 pairs of RNA-protein used for positive controls are LET7 vs. LIN28a, IRE vs. IRP1, HCV3′UTR vs. RPL22. We want to thank David E. Hill and Marc Vidal for helping set up the Y3H screens and for the DFCI-hORF8.1 collection.

RNA-immunoprecipitation: For RNA immunoprecipitation (RNA-IP), HEK293T E2F1-HiBiT cells were generated by knock-in of a HiBiT tag at the endogenous E2F1 locus to express E2F1 with a C-terminal HiBiT tag linked via Val-Ser. HiBiT-tag knock-in was performed by electroporation with Cas9-gRNA ribonucleotide complex and a single-stranded HDR template with 80-nucleotide homology arms using the Lonza 4D Nucleofector and the SF Cell Line 4D-Nucleofector X Kit S (Lonza, V4XC-2032). Nucleofection protocol was adapted from[71] and all Alt-R reagents were purchased from IDT (See Table 2). Briefly, 120 pmol Alt-R CRISPR-Cas9 crRNA (E2F1-g2) was annealed to 120 pmol Alt-R CRISPR-Cas9 tracrRNA and subsequently mixed with 10 μL SF nucleofection solution. The gRNA solution was added to 100 pmol Alt-R S.p. Cas9 Nuclease V3 and 100 pmol Alt-R HDR Donor Oligo (ssODN2_E2F1-Cterm_5arm-Val-Ser-HiBiT-3arm) with a final concentration of 3.2% (v/v) glycerol and incubated at RT for 15 min 100,000 cells in 10 μL SF nucleofection solution were added to the RNP mix and electroporated. Immediately after electroporation, 80 μL DMEM containing 10% FBS was added to the cells and after 10 min incubation at RT, cells were plated in 2 mL DMEM containing 10% FBS. To isolate single clones, single cells were sorted into 96-well plates. Single clones with HiBiT integration were identified by screening for luminescence using

the Nano-Glo HiBiT Lytic Detection System (Promega, N3030) according to the provided protocol. Clones were further characterized by isolating gDNA, PCR amplification of the integration site (amplicon primer: E2F1-HiBiT-amplf and E2F1-HiBiT-amplr) and Sanger sequencing (sequencing primer: E2F1ampl-seqr, Azenta). The single clone used for RNA-IP is partially HiBiT-tagged.

RNA-IP and qPCR (RIP-qPCR) was performed as described in[72] with slight modifications. Briefly, 5 x10 HEK293T-E2F1-HiBiT cells were seeded in 15 cm dishes in DMEM media completed with 10% FBS. After 12h the cells were transfected with 10 ng of *SLNCR* overexpression vector using lipofectamine 2000 transfection reagent and following manufacturer's protocol. The cells were harvested 48h post transfection, washed in ice-cold PBS and lysed in lysis buffer (20 mM Tris-HCl pH 7.5, 100 mM KCl, 5 mM $MgCl_2$, 0.5% NP-40) freshly supplemented with (cOmplete Protease Inhibitor Cocktail and 40 U/mL of RNaseOUT). The lysate was cleared by centrifugation and quantified by BCA assay. The lysate was normalized to 1 mg/mL protein content and applied onto pre-antibody coated magnetic protein-G Dynabeads, using 2 μg of antibody per IP sample. The IP mix was brought to 3 mL final volume in NT2 buffer (50 mM Tris HCl pH 7.5, 150 mM NaCl, 1 mM $MgCl_2$, 0.05% NP-40) and supplemented with 1 μM of DTT and 16.5 μM EDTA pH 8.0. Immunoprecipitation was conducted with either anti HiBiT antibody or normal mouse IgG as a control. Immunoprecipitation reactions were allowed to run for 4 h at 4° with rotation. The samples were then washed 5 times in NT2 buffer. The samples were treated with Turbo DNAse to digest out any DNA contaminants for 1h at 37°C and washed again once with NT2 buffer. Finally, the co-precipitated RNA was extracted from the beads by incubating the sample with 5 μg of proteinase K in 100 μL of NT2 buffer (without protease inhibitors) supplemented with 40 U/mL of RNaseOUT and 0.1% SDS. The remaining RNA was purified from the bead supernatant containing proteinase K by phenol:chloroform:isoamyl alcohol extraction and subsequently reverse transcribed and used for qPCR as described below.

RNA extraction and cDNA library preparation and qPCR: RNA was isolated using RNeasy plus Mini Kit (Qiagen, 74134) following manufacturer's protocol and sent to Azenta (Genewiz) for library preparation (Illumina, rRNA depletion) and sequencing (Illumina HiSeq 2x 150bp configuration, single index per lane). cDNA was generated using SuperScript III (Invitrogen, 18080093) reverse transcriptase following manufacturer's protocol. The indicated transcripts were quantified using SsoAdvanced Universal SYBR Green SuperMix (BioRad, 1725271) on a CFX384 Touch RealTime PCR Detection System.

RNA-seq, TF enrichment analysis, survival plots, and disease Associated Transcriptional network analysis (DATNA): Raw sequencing reads were quality-checked using FastQC (v0.11.5) (https://www.bioinformatics.babraham.ac.uk/projects/fastqc/) and data were pre-processed with Cutadapt (v2.5)[73] for adapter removal following best practices.[64] Gene expression quantification was performed by aligning against the GRCm38 genome using STAR (v2.7.3a)[65] and quantifying reads against Ensembl v98[74] annotated transcript loci with featureCounts (Subread 1.6.2).[69] Differential gene

expression analysis was performed using DESeq2 (v1.24.0).[66] The raw data is deposited to GSE270372.

TF analysis: The DIANA-mirExTra v2.0[67] suite supports differentially expression analysis from bulk RNA-Seq and small RNA-Seq data, giving users several options for statistical analysis. Differential expression analysis was performed using the R package DESeq2 (v.1.24.07)[66] within the online suite, comparing the Full-length and Empty SLNCR genotypes. Differentially expressed regulators and potential targets, that had an adjusted *p*-value below 0.05, were handpicked for the second step of the analysis, annotation and analysis of the TFBS by DIANA-mirExTra.

DIANA-mirExTra gathers TFBS data from in-house analyzed DNAse-Seq datasets and community curated entries from the ORegAnno v3.0 database (http://www.oreganno.org/).[75] Binding coordinates and annotation were derived from the miRGen v3.0 database.[76] For the purposes of this analysis, our lab took possible differentially expressed targets within and around these curated TFBS regions. After annotating TFBS and combining them with nearby targets, we utilized the DIANA-mirExTra R scripts (R 3.6.0) to perform an overrepresentation analysis (Fisher exact test) based on the hypergeometric distribution. TFs with a statistically significant number of targets in proximity of its binding site, were kept and highlighted in the results. Differentially expressed targets were annotated using the ensembl 80 database, from the GRCh38 version of the human genome.

Survival plots: The survival analysis was performed using the TCGA Pan-Cancer Clinical Data Resource (TCGA-CDR)[77] as well as the publicly available RNA-seq expression data from the Genomic Data Commons (GDC) TCGA Skin Cutaneous Melanoma patient cohort [https://docs.gdc.cancer.gov/Data/Bioinformatics_Pipelines/Expression_mRNA_Pipeline/] to assess the effect of SLNCR and E2F1 expression on overall patient survival. The FPKM normalized expression values were used to stratify patients based on the expression of *SLNCR* and E2F1. The analysis was performed in R [R Core Team. R: A language and environment for statistical computing. Vienna, Austria: R Foundation for Statistical Computing; 2023. Available: https://www.R-project.org/] using the ggsurvfit [Sjoberg DD, Baillie M, Fruechtenicht C, Haesendonckx S, Treis T. Ggsurvfit: Flexible time-to-event figures. 2023. Available: https://CRAN.R-project.org/package=ggsurvfit] and survminer [Kassambara A, Kosinski M, Biecek P. Survminer: Drawing survival curves using 'ggplot2'. 2021. Available: https://CRAN.R-project.org/package=survminer] packages. Following the recommendations of,[77] the survival analysis focused on the primary tumor samples and overall survival (OS) as the endpoint. Furthermore, the follow-up time was adjusted by considering the sample acquisition date. Hence, only samples with a valid sample acquisition date and without 'Metastasis' in the tumor tissue site description were included ($n = 76$).

The DATNA algorithm was run on Melanoma (SKCM version available as of 2019) TCGA transcriptomic database with SLNCR as the lncRNA, the Y3H orfeome-wide identified SLNCR binders as the considered partners, and the differentially expressed genes between full-length SLNCR and Empty plasmid control (FDR <0.005, see Table S1) as the potential target genes; with the following parameters: (i) Top and bottom 20th percentiles of SLNCR

expression for patient samples group selection (pct = 0.2); and (ii) minimum difference of 0.3 in target and TF spearman correlations between patient sample groups (d > 0.3). Disease relevant target genes (expressed and with some variation) were filtered in by having a minimum combined expression of at least 50 TPM (sum >50) and a minimum standard deviation of 10 (sd > 10). The code to run the algorithm in R is deposited at Zenodo. Please see Resource availability section.

E2F1 DNA binding domain protein purification: Expression and purification of E2F1 DNA-binding domain was carried out as previously described[78] with the following modifications. After elution, protein was concentrated using Amicon Ultracentrifugation filter 10 kDa by spinning at 4000 g for 15 min.

RNA/DNA electrophoretic mobility shift assays (R/EMSA): For the 42-mer dsDNA oligo, the complimentary strands were annealed to equimolar ratios of corresponding unlabeled oligonucleotides in NEB Buffer 2 (NEB, B7002S) for 5 min at 95°C, 10 min at 70°C and cooled down to 4 °C at the rate of 1 °C/min. REMSA was performed using Thermo Fisher Scientific LightShift Chemiluminescent RNA EMSA (REMSA) Kit (Thermo Fisher Scientific, 20158) following manufacturer's protocol. Briefly, 20 μL binding reactions were assembled in low-adhesion tubes (Costar, 3207) in 1X binding buffer (10 mM HEPES pH 7.3, 20 mM KCl, 1 mM $MgCl_2$, 1 mM DTT), with 2 μg of yeast tRNA, the indicated amount of recombinant full length E2F1 (Abcam, ab82207) or E2F1 DNA binding domain (see $E2F1^{DBD}$ purification), various final concentrations of the biotinylated *SLNCR* or 42-mer dsDNA oligos as indicated, and/or 5–10 μM of unlabeled *SLNCR* oligos or 42-mer dsDNA where indicated. Reactions were incubated at room temperature for 30 min, then mixed with 5 μL of 5X Novex TBE (Invitrogen, LC6678) loading dye, and 20 μL of this mix were electrophoresed on 5% Mini-PROTEAN TBE Gel, 12 well, 20 μL (Bio-Rad 4565015). R/DNA and protein/R/DNA complexes were transferred to Amersham Hybond –N + Membrane (to GE Healthcare, 45–000) in 0.5X TBE at 400 mA for 30 min using the Bio-Rad Wet Transfer System. Detection was performed according to LightShift REMSA kit, using ChemiDoc XRS+ System (Bio-Rad). In the case of $E2F1^{DBD}$ binding to DNA fragment, reactions were assembled as above and electrophoresed as above but the DNA fragment used was 5′-labeled with γ^{-} P-ATP instead of 3′-biotin labeled. After electrophoresis, the gel was dried for 40 min at 65°C. The dried gel was exposed to a film overnight and imaged the next day using Amersham Typhoon Imager. The 3′-biotin labeled RNA and DNA oligos and unlabeled oligos were ordered from IDT. The RNA Mimic 2 + 3 oligos were synthesized by AUM BioTech, LLC (Philadelphia, PA).

RESOURCE AVAILABILITY

Lead contact

Requests for further information and resources should be directed to and will be fulfilled by the lead contact, Carl D. Novina (carl_novina@dfci.harvard.edu).

Materials availability

All unique/stable reagents generated in this study are available from the lead contact with a completed materials transfer agreement.

Data and code availability

- RNA-seq data have been deposited at GEO: GSE270372 and are publicly available as of the date of publication.
- All original code has been deposited at Zenodo at https://doi.org/10.5281/zenodo.15008289 and is publicly available as of the date of publication.

REMSA to assess relative binding affinity of E2F1 to SLCNR fragments was performed with 12.5, 25, 50, 100, 200 nM of 3′-biotin labeled RNA oligonucleotides, incubated with 0.5 μg (0.5 μM) or recombinant E2F1. Additionally, labeled BS2+3 oligonucleotide was incubated with increasing amounts of E2F1 from 0.085 to 0.5 μM,

REMSA to detect E2F1 binding to single binding sites was performed with 200 nM of 3′-biotin labeled RNA oligonucleotides resembling single *SLNCR* E2F1 binding sites (BS) as single stranded, double stranded or hybrid fragments, incubated with 0.5 μg (0.5 μM) of recombinant E2F1.

REMSA to detect E2F1 binding to double binding sites was performed using 200 nM 3′-biotin labeled single sites or 50 nM biotinylated double sites or 10 μM unlabeled versions of above RNA oligonucleotides containing specified single or double *SLNCR* E2F1 binding sites were incubated with 0.5 μg E2F1.

REMSA for competition assays with full-length E2F1 was performed using 100 nM of 3′-biotin labeled 42-mer dsDNA oligonucleotides and 50 nM to 30 μM of unlabeled RNA oligonucleotides (*SLNCR* BS2+3) incubated with 0.5 μg E2F1 or vice versa with 50 nM of 3′-biotin labeled *SLNCR* BS2+3 and 500 nM to 500 μM unlabeled DNA oligo. 10 μM unlabeled oligonucleotide of the same species as the labeled nucleotide was used to show specific binding. REMSA for competition assays with $E2F1^{DBD}$ was performed using 1 μM of 3′-biotin labeled 42-mer dsDNA and 250 nM to 2.5 μM of unlabeled *SLNCR* BS2+3 incubated with purified 0.5 μg (0.5 μM) $E2F1^{DBD}$ or vice versa incubated with 2.25 μM–36.6 μM unlabeled 42-mer dsDNA. 18 μM unlabeled 42-mer dsDNA oligonucleotide or 5 μM of unlabeled BS2+3 RNA was used to show specific binding.

REMSA to detect mutant $E2F1^{DBD}$ binding to *SLNCR* were performed using 50 nM of $^{\gamma-}$P-labelled 42-mer DNA or 3′-biotin labeled BS2+3 RNA oligonucleotides incubated with purified 0.5 μg (0.5 μM) wild type or mutant (R166H or L132E) $E2F1^{DBD}$.

REMSA to detect E2F1+DP1 binding to *SLNCR* were performed using 50 nM of 3′-biotin labeled BS2+3 RNA incubated with 0.5 μg E2F1 or 2 μg DP1 or both with increasing amounts of DP1 (0.2–2 μg).

REMSA to detect E2F1 binding to RNA Mimic 2 + 3 was performed using 50 nM SCR or E2F1-mimic oligo and 0.5 μg E2F1.

Mouse studies: The mouse experiment was performed under Dana-Farber Institutional Animal Care and Use Committee (IACUC) approved protocol #23-001. 0.2x10 *SLNCR* over-expressing A375 cells transfected with 1 μM Scr or RNA Mimic 2 + 3 (an oligo that blocks E2F1-*SLNCR* interactions) for 48 h. Treated cells were then washed twice with 1X PBS before resuspending in 100 μL 1X PBS. Cells were then injected into mice tail vein. Injections and bioluminescence imaging (BLI) was performed at DFCI Animal Resources Facility. Tumor growth was monitored weekly or twice a week by BLI using the IVIS Spectrum *In Vivo* Imaging System (PerkinElmer). Briefly, mice were injected subcutaneously with 75 mg/kg D-luciferin potassium salt (Promega E1605) in sterile PBS and anesthetized with 2% isoflurane in medical air. Serial bioluminescence images

were acquired using the automated exposure set-up. The peak bioluminescence signal intensity within selected regions of interest (ROIs) was quantified using the Living Image Software (PerkinElmer) and expressed as photon flux (p/sec/cm2/sr). Representative planar bioluminescence images were displayed with indicated adjusted minimal and maximal thresholds.

Molecular dynamics simulation: The starting configurations for the molecular dynamics trajectories were based on the E2F4/DP2/DNA (PDB ID 1CF7)[25] system and the DNA binding domains (DBD) of E2F1 (residues 120–205) and DP1 (residues 103–204) modeled using the model in AlphaFold2DB. The DBDs of E2F1 and DP1 aligned on the corresponding peptides E2F4 and DP2 in the DNA bound complex resulted in 0.73 Aand 1.03 Å root mean squared deviations (RMSD) for the backbone atoms. There were multiple systems prepared: Various systems used in the study are given in Table 1 with the number of Na^+ and Cl^- ions used to provide the 100 mM effective ionic concentration, plus the charge neutralization. Also, the total number of water molecules in each system was given in this table. When each system was solvated in a box of TIP3P water, the box boundary was selected to extend 20 A from the nearest peptide atom. All Lys, Arg, Glu and Asp residues are in their charged states. Histidine residues were deemed ε-protonated (according to Molprobity check).[79] 15-mer reference double stranded DNA is the DNA found in the X-ray structure in 1CF7.The 42-mer dsDNA is the 42 nucleotide double stranded DNA (total 84 nucleotides) used in the experiments. The 60-mer *SLNCR* RNA in the table is the DNA in the X-crystal structure (1CF7) converted to RNA by adding 2′ hydroxyl groups to the sugars. 60-mer RNA is the RNA designated as “binding site 2 + 3” in the experiments. Prior to equilibration, each solvated system was sequentially subjected to 1) 500 ps belly dynamics with fixed peptide, 2) minimization (5,000 steps), 3) constant temperature (200 K) - constant pressure (1 atm) dynamics (~1 ns) at fixed protein to assure a reasonable starting density around 1 g/cc, 4) minimization (5,000 steps), 5) stepwise heating MD at constant volume (to bring the temperature up to 300 K in 3 ns), and 6) constant volume simulation for 10ns with a constraint force constant of 10 kcal/mol applied only on backbone heavy atoms. After releasing all constraining forces within the next 20ns of the equilibration period, sampling was increased by performing 3 independent, constant-temperature (Langevin thermostat) constant-volume (NVT) molecular dynamics simulations for 1 μs each. However, for systems with RNA only, simulations were not triplicated. All trajectories were calculated using the PMEMD module of Amber.20 with 2 fs time step. Long range coulombic interactions were handled using the PME method with a 10 A cut-off for the direct interactions. The amino acid parameters were selected from the FF14SB force field of Amber.20, the DNA forcefield was selected from the Parmbsc1 parameters and RNA forcefield was from the RNA.OL3 parameters in Amber.20. At the salt concentration of 100 mM, the MMGBSA module with the standard parameters was used to estimate binding energies from 1,000 samples selected from molecular dynamics simulations at each nanosecond interval and combining all the sample runs for each system.

DMS-probing of *SLNCR*: DMS-probing was performed as described in[21] with small modifications. Briefly, 0.5x10 A375 cells, stably overexpressing *SLNCR* were seeded in 15 cm dishes. At 80–90% confluency, the media was removed and replaced with fresh

media supplemented with 2% fresh DMS (Sigma, D2650) probing media. Probing media was then removed, and the cells were rinsed twice in PBS supplemented with 30% v/v β-mercaptoethanol and then once with PBS. Cells were harvested by light scraping and collected by centrifugation at 1,500 rpm for 5 min at 4°C. RNA was extracted following the TRIzol (Invitrogen, 15596026) method and resuspended in 50 μL of nuclease-free water. 5 μg of RNA were digested with TURBO DNase (Invitrogen, AM2238) following manufacturer's protocol and then the RNA was re-extracted by ethanol precipitation. The pure, DNA-free RNA was quantified by nanodrop, and the concentration was adjusted to 150 ng/μL 750 ng of RNA were reverse transcribed with Induro reverse transcriptase (NEB, M0681) with specific primers (see Table 2) following manufacturer's protocol and with extension time for 3 h. Induro RT is the commercially available equivalent of the marathon RT recommended by the published protocol. Samples were cleaned up by Zymogen DNA Clean & Concentrator-5 columns following the alkaline hydrolysis method for RNA removal. Samples were then amplified by PCR covering the majority of SLNCR in overlapping fragments. The PCR amplicons were purified from a 6% DNA retardation TBE-acrylamide gel and extracted by the crush-soak method. The purified DNA fragments were quality controlled by Tapestation D1000 electrophoresis (Agilent, 5067–5582 and 5067–5583). Library preparation and Next-generation sequencing were performed by Azenta. Raw fastq files were analyzed and DMS reactivities calculated by ShapeMapper 2.[62] Correlation analysis of the per nucleotide DMS reactivities across biological replicates were calculated by Spearman's correlation ranking test using GraphPad Prism 10 (version 10.1.1).

***In silico* RNA folding for full length and fragments of *SLNCR*:** Secondary structure predictions were performed using the RNAFold version 6.4[19,20] accessed via the Matthews lab webserver. The sequences of full length *SLNCR* or *SLNCR* fragment s were uploaded as fasta files. Parameters used for the fold algorithm were as follows: Maximum % Energy Difference 10, Maximum Loop Size 30, window size 3, temperature 310.15 K. For full length *SLNCR* DMS-probing reactivities as calculated by ShapeMapper 2 were input as the SHAPE constraints file. The most thermodynamically stable structure maps of full length *SLNCR* or its fragments were saved as.ct files and visualised using VARNA.[63] Graphic representations were created using Adobe Illustrator 2024.

Immunoblotting and antibodies: A375 cells were boiled in 2X Laemmli buffer (BioRad, 1610737) with 2-BME for 10 min. Samples were separated on 12% Mini-PROTEAN TGX Precast Protein Gels (BioRad, 4561045EDU) and transferred to Nitrocellulose 0.2 μm membrane (BioRad, 1620146) using manufacturer's protocol for wet transfer in Mini-Protean Tetra Cell tank (BioRad, 1658029). The following antibodies were used: Cyclophilin B (Cell Signaling, Technologies D1V5J) at 1:500 and E2F1 (Cell Signaling Technologies, 3472) at 1:500.

QUANTIFICATION AND STATISTICAL ANALYSIS

Significance was calculated by T tests, ANOVA (for multiple comparisons) and correlation analysis (for the DMS-probing data) were performed using GraphPad Prism (version 9.00). In proliferation and invasion assays error bars represent the mean ± SD of 3 independent

replicates. RT-qPCR data is represented as the fold change compared to scramble control, normalized to B-ACT. Error bars represent standard deviations calculated from 3 reactions.

Supplementary Material

Refer to Web version on PubMed Central for supplementary material.

ACKNOWLEDGMENTS

We wish to thank Dr. Panagiotis Kakoulidis and Dr. Thomas Walz for critically reading this manuscript. This work was supported by NIH grants R01HL145714 and DP1DK126161 to C.D.N., by NCI R01CA258776 to I.S.V., and by Swiss National Science Foundation Fellowships P2EZP3_184225 and P400PB_194396 to S.S. This study was partly supported by the Division of Intramural Research of the National Institute of Environmental Health Sciences, NIH, research project ZIA ES43010 to L.P.

REFERENCES

1. Kent LN, and Leone G (2019). The broken cycle: E2F dysfunction in cancer. Nat. Rev. Cancer 19, 326–338. 10.1038/s41568-019-0143-7. [PubMed: 31053804]
2. Meng P, and Ghosh R (2014). Transcription addiction: can we garner the Yin and Yang functions of E2F1 for cancer therapy? Cell Death Dis. 5, e1360. 10.1038/cddis.2014.326. [PubMed: 25101673]
3. Komori H, Goto Y, Kurayoshi K, Ozono E, Iwanaga R, Bradford AP, Araki K, and Ohtani K (2018). Differential requirement for dimerization partner DP between E2F-dependent activation of tumor suppressor and growth-related genes. Sci. Rep 8, 8438. 10.1038/s41598-018-26860-0. [PubMed: 29855511]
4. Kohn MJ, Leung SW, Criniti V, Agromayor M, and Yamasaki L (2004). Dp1 is largely dispensable for embryonic development. Mol. Cell Biol 24, 7197–7205. 10.1128/MCB.24.16.7197-7205.2004. [PubMed: 15282318]
5. Rubin SM, Gall AL, Zheng N, and Pavletich NP (2005). Structure of the Rb C-terminal domain bound to E2F1-DP1: a mechanism for phosphorylation-induced E2F release. Cell 123, 1093–1106. 10.1016/j.cell.2005.09.044. [PubMed: 16360038]
6. Blanchet E, Annicotte JS, Lagarrigue S, Aguilar V, Clapé C, Chavey C, Fritz V, Casas F, Apparailly F, Auwerx J, and Fajas L (2011). E2F transcription factor-1 regulates oxidative metabolism. Nat. Cell Biol 13, 1146–1152. 10.1038/ncb2309. [PubMed: 21841792]
7. Altintas DM, Shukla MS, Goutte-Gattat D, Angelov D, Rouault JP, Dimitrov S, and Samarut J (2012). Direct cooperation between androgen receptor and E2F1 reveals a common regulation mechanism for androgen-responsive genes in prostate cells. Mol. Endocrinol 26, 1531–1541. 10.1210/me.2012-1016. [PubMed: 22771493]
8. Galbiati L, Mendoza-Maldonado R, Gutierrez MI, and Giacca M (2005). Regulation of E2F-1 after DNA damage by p300-mediated acetylation and ubiquitination. Cell Cycle 4, 930–939. 10.4161/cc.4.7.1784. [PubMed: 15917652]
9. Taubert S, Gorrini C, Frank SR, Parisi T, Fuchs M, Chan HM, Livingston DM, and Amati B (2004). E2F-dependent histone acetylation and recruitment of the Tip60 acetyltransferase complex to chromatin in late G1. Mol. Cell Biol 24, 4546–4556. 10.1128/MCB.24.10.4546-4556.2004. [PubMed: 15121871]
10. Rouaud F, Hamouda-Tekaya N, Cerezo M, Abbe P, Zangari J, Hofman V, Ohanna M, Mograbi B, El-Hachem N, Benfodda Z, et al. (2018). E2F1 inhibition mediates cell death of metastatic melanoma. Cell Death Dis. 9, 527. 10.1038/s41419-018-0566-1. [PubMed: 29743521]
11. Schmidt K, Joyce CE, Buquicchio F, Brown A, Ritz J, Distel RJ, Yoon CH, and Novina CD (2016). The lncRNA SLNCR1 Mediates Melanoma Invasion through a Conserved SRA1-like Region. Cell Rep. 15, 2025–2037. 10.1016/j.celrep.2016.04.018. [PubMed: 27210747]
12. Schmidt K, Buquicchio F, Carroll JS, Distel RJ, and Novina CD (2017). RATA: A method for high-throughput identification of RNA bound transcription factors. J. Biol. Methods 4, e67. 10.14440/jbm.2017.171. [PubMed: 29201933]

13. Schmidt K, Weidmann CA, Hilimire TA, Yee E, Hatfield BM, Schneekloth JS Jr., Weeks KM, and Novina CD (2020). Targeting the Oncogenic Long Non-coding RNA SLNCR1 by Blocking Its Sequence-Specific Binding to the Androgen Receptor. Cell Rep. 30, 541–554.e5. 10.1016/j.celrep.2019.12.011. [PubMed: 31940495]

14. Schmidt K, Carroll JS, Yee E, Thomas DD, Wert-Lamas L, Neier SC, Sheynkman G, Ritz J, and Novina CD (2019). The lncRNA SLNCR Recruits the Androgen Receptor to EGR1-Bound Genes in Melanoma and Inhibits Expression of Tumor Suppressor p21. Cell Rep. 27, 2493–2507.e4. 10.1016/j.celrep.2019.04.101. [PubMed: 31116991]

15. Thandapani P, O'Connor TR, Bailey TL, and Richard S (2013). Defining the RGG/RG motif. Mol. Cell 50, 613–623. 10.1016/j.molcel.2013.05.021. [PubMed: 23746349]

16. Long Y, Wang X, Youmans DT, and Cech TR (2017). How do lncRNAs regulate transcription? Sci. Adv 3, eaao2110. 10.1126/sciadv.aao2110. [PubMed: 28959731]

17. Sengupta DJ, Wickens M, and Fields S (1999). Identification of RNAs that bind to a specific protein using the yeast three-hybrid system. RNA 5, 596–601. 10.1017/s1355838299002113. [PubMed: 10199575]

18. SenGupta DJ, Zhang B, Kraemer B, Pochart P, Fields S, and Wickens M (1996). A three-hybrid system to detect RNA-protein interactions in vivo. Proc. Natl. Acad. Sci. USA 93, 8496–8501. [PubMed: 8710898]

19. Mathews DH (2004). Using an RNA secondary structure partition function to determine confidence in base pairs predicted by free energy minimization. RNA 10, 1178–1190. 10.1261/rna.7650904. [PubMed: 15272118]

20. Reuter JS, and Mathews DH (2010). RNAstructure: software for RNA secondary structure prediction and analysis. BMC Bioinf. 11, 129. 10.1186/1471-2105-11-129.

21. Zubradt M, Gupta P, Persad S, Lambowitz AM, Weissman JS, and Rouskin S (2017). DMS-MaPseq for genome-wide or targeted RNA structure probing in vivo. Nat. Methods 14, 75–82. 10.1038/nmeth.4057. [PubMed: 27819661]

22. Craft N, Bruhn KW, Nguyen BD, Prins R, Liau LM, Collisson EA, De A, Kolodney MS, Gambhir SS, and Miller JF (2005). Bioluminescent imaging of melanoma in live mice. J. Invest. Dermatol 125, 159–165. 10.1111/j.0022-202X.2005.23759.x. [PubMed: 15982316]

23. Hellman LM, and Fried MG (2007). Electrophoretic mobility shift assay (EMSA) for detecting protein-nucleic acid interactions. Nat. Protoc 2, 1849–1861. 10.1038/nprot.2007.249. [PubMed: 17703195]

24. Jumper J, Evans R, Pritzel A, Green T, Figurnov M, Ronneberger O, Tunyasuvunakool K, Bates R, Žídek A, Potapenko A, et al. (2021). Highly accurate protein structure prediction with AlphaFold. Nature 596, 583–589. 10.1038/s41586-021-03819-2. [PubMed: 34265844]

25. Zheng N, Fraenkel E, Pabo CO, and Pavletich NP (1999). Structural basis of DNA recognition by the heterodimeric cell cycle transcription factor E2F-DP. Genes Dev. 13, 666–674. 10.1101/gad.13.6.666. [PubMed: 10090723]

26. Tao Y, Kassatly RF, Cress WD, and Horowitz JM (1997). Subunit composition determines E2F DNA-binding site specificity. Mol. Cell Biol 17, 6994–7007. 10.1128/MCB.17.12.6994. [PubMed: 9372931]

27. Yu W, Chan-On W, Teo M, Ong CK, Cutcutache I, Allen GE, Wong B, Myint SS, Lim KH, Voorhoeve PM, et al. (2011). First somatic mutation of E2F1 in a critical DNA binding residue discovered in well-differentiated papillary mesothelioma of the peritoneum. Genome Biol. 12, R96. 10.1186/gb-2011-12-9-r96. [PubMed: 21955916]

28. Woods K, Thomson JM, and Hammond SM (2007). Direct regulation of an oncogenic micro-RNA cluster by E2F transcription factors. J. Biol. Chem 282, 2130–2134. 10.1074/jbc.C600252200. [PubMed: 17135268]

29. Roworth AP, Carr SM, Liu G, Barczak W, Miller RL, Munro S, Kanapin A, Samsonova A, and La Thangue NB (2019). Arginine methylation expands the regulatory mechanisms and extends the genomic landscape under E2F control. Sci. Adv 5, eaaw4640. 10.1126/sciadv.aaw4640. [PubMed: 31249870]

30. Cassiday LA, and Maher LJ 3rd. (2002). Having it both ways: transcription factors that bind DNA and RNA. Nucleic Acids Res. 30, 4118–4126. 10.1093/nar/gkf512. [PubMed: 12364590]

31. Holmes ZE, Hamilton DJ, Hwang T, Parsonnet NV, Rinn JL, Wuttke DS, and Batey RT (2020). The Sox2 transcription factor binds RNA. Nat. Commun 11, 1805. 10.1038/s41467-020-15571-8. [PubMed: 32286318]
32. Hou L, Wei Y, Lin Y, Wang X, Lai Y, Yin M, Chen Y, Guo X, Wu S, Zhu Y, et al. (2020). Concurrent binding to DNA and RNA facilitates the pluripotency reprogramming activity of Sox2. Nucleic Acids Res. 48, 3869–3887. 10.1093/nar/gkaa067. [PubMed: 32016422]
33. Saldana-Meyer R, Rodriguez-Hernaez J, Escobar T, Nishana M, Jacome-Lopez K, Nora EP, Bruneau BG, Tsirigos A, Furlan-Magaril M, Skok J, and Reinberg D (2019). RNA Interactions Are Essential for CTCF-Mediated Genome Organization. Mol. Cell 76, 412–422.e415. 10.1016/j.molcel.2019.08.015. [PubMed: 31522988]
34. Sigova AA, Abraham BJ, Ji X, Molinie B, Hannett NM, Guo YE, Jangi M, Giallourakis CC, Sharp PA, and Young RA (2015). Transcription factor trapping by RNA in gene regulatory elements. Science 350, 978–981. 10.1126/science.aad3346. [PubMed: 26516199]
35. Theunissen O, Rudt F, Guddat U, Mentzel H, and Pieler T (1992). RNA and DNA binding zinc fingers in Xenopus TFIIIA. Cell 71, 679–690. 10.1016/0092-8674(92)90601-8. [PubMed: 1423623]
36. Xu Y, Huangyang P, Wang Y, Xue L, Devericks E, Nguyen HG, Yu X, Oses-Prieto JA, Burlingame AL, Miglani S, et al. (2021). ERalpha is an RNA-binding protein sustaining tumor cell survival and drug resistance. Cell 184, 5215–5229.e5217. 10.1016/j.cell.2021.08.036. [PubMed: 34559986]
37. Jeon Y, and Lee JT (2011). YY1 tethers Xist RNA to the inactive X nucleation center. Cell 146, 119–133. 10.1016/j.cell.2011.06.026. [PubMed: 21729784]
38. Yoshida Y, Izumi H, Torigoe T, Ishiguchi H, Yoshida T, Itoh H, and Kohno K (2004). Binding of RNA to p53 regulates its oligomerization and DNA-binding activity. Oncogene 23, 4371–4379. 10.1038/sj.onc.1207583. [PubMed: 15064727]
39. Steiner HR, Lammer NC, Batey RT, and Wuttke DS (2022). An Extended DNA Binding Domain of the Estrogen Receptor Alpha Directly Interacts with RNAs in Vitro. Biochemistry 61, 2490–2494. 10.1021/acs.biochem.2c00536. [PubMed: 36239332]
40. Niessing D, Driever W, Sprenger F, Taubert H, Jäckle H, and Rivera-Pomar R (2000). Homeodomain position 54 specifies transcriptional versus translational control by Bicoid. Mol. Cell 5, 395–401. 10.1016/s1097-2765(00)80434-7. [PubMed: 10882080]
41. Dvir S, Argoetti A, Lesnik C, Roytblat M, Shriki K, Amit M, Hashimshony T, and Mandel-Gutfreund Y (2021). Uncovering the RNA-binding protein landscape in the pluripotency network of human embryonic stem cells. Cell Rep. 35, 109198. 10.1016/j.celrep.2021.109198. [PubMed: 34077720]
42. Wang X, Zhao S, Xin Q, Zhang Y, Wang K, and Li M (2024). Recent progress of CDK4/6 inhibitors' current practice in breast cancer. Cancer Gene Ther. 31, 1283–1291. 10.1038/s41417-024-00747-x. [PubMed: 38409585]
43. Hood FE, Sahraoui YM, Jenkins RE, and Prior IA (2023). Ras protein abundance correlates with Ras isoform mutation patterns in cancer. Oncogene 42, 1224–1232. 10.1038/s41388-023-02638-1. [PubMed: 36864243]
44. Nevins JR (2001). The Rb/E2F pathway and cancer. Hum. Mol. Genet 10, 699–703. 10.1093/hmg/10.7.699. [PubMed: 11257102]
45. Llombart V, and Mansour MR (2022). Therapeutic targeting of "undruggable" MYC. EBioMedicine 75, 103756. 10.1016/j.ebiom.2021.103756. [PubMed: 34942444]
46. Piunti A, and Shilatifard A (2021). The roles of Polycomb repressive complexes in mammalian development and cancer. Nat. Rev. Mol. Cell Biol 22, 326–345. 10.1038/s41580-021-00341-1. [PubMed: 33723438]
47. Davidovich C, and Cech TR (2015). The recruitment of chromatin modifiers by long noncoding RNAs: lessons from PRC2. RNA 21, 2007–2022. 10.1261/rna.053918.115. [PubMed: 26574518]
48. Portoso M, Ragazzini R, Brenčič Ž, Moiani A, Michaud A, Vassilev I, Wassef M, Servant N, Sargueil B, and Margueron R (2017). PRC2 is dispensable for HOTAIR-mediated transcriptional repression. EMBO J. 36, 981–994. 10.15252/embj.201695335. [PubMed: 28167697]
49. Hajjari M, and Salavaty A (2015). HOTAIR: an oncogenic long non-coding RNA in different cancers. Cancer Biol. Med 12, 1–9. 10.7497/j.issn.2095-3941.2015.0006. [PubMed: 25859406]

50. Yang J, Qi M, Fei X, Wang X, and Wang K (2021). Long non-coding RNA XIST: a novel oncogene in multiple cancers. Mol. Med 27, 159. 10.1186/s10020-021-00421-0. [PubMed: 34930117]
51. Oksuz O, Henninger JE, Warneford-Thomson R, Zheng MM, Erb H, Vancura A, Overholt KJ, Hawken SW, Banani SF, Lauman R, et al. (2023). Transcription factors interact with RNA to regulate genes. Mol. Cell 83, 2449–2463.e13. 10.1016/j.molcel.2023.06.012. [PubMed: 37402367]
52. Jordan KL, Haas AR, Logan TJ, and Hall DJ (1994). Detailed analysis of the basic domain of the E2F1 transcription factor indicates that it is unique among bHLH proteins. Oncogene 9, 1177–1185. [PubMed: 8134120]
53. Hossain SM, and Eccles MR (2023). Phenotype Switching and the Melanoma Microenvironment; Impact on Immunotherapy and Drug Resistance. Int. J. Mol. Sci 24, 1601. 10.3390/ijms24021601. [PubMed: 36675114]
54. Ishizaki J, Nevins JR, and Sullenger BA (1996). Inhibition of cell proliferation by an RNA ligand that selectively blocks E2F function. Nat. Med 2, 1386–1389. 10.1038/nm1296-1386. [PubMed: 8946842]
55. Hook B, Bernstein D, Zhang B, and Wickens M (2005). RNA-protein interactions in the yeast three-hybrid system: affinity, sensitivity, and enhanced library screening. RNA 11, 227–233. 10.1261/rna.7202705. [PubMed: 15613539]
56. James P, Halladay J, and Craig EA (1996). Genomic libraries and a host strain designed for highly efficient two-hybrid selection in yeast. Genetics 144, 1425–1436. 10.1093/genetics/144.4.1425. [PubMed: 8978031]
57. Lam AJ, St-Pierre F, Gong Y, Marshall JD, Cranfill PJ, Baird MA, McKeown MR, Wiedenmann J, Davidson MW, Schnitzer MJ, et al. (2012). Improving FRET dynamic range with bright green and red fluorescent proteins. Nat. Methods 9, 1005–1012. 10.1038/nmeth.2171. [PubMed: 22961245]
58. Veggiani G, Nakamura T, Brenner MD, Gayet RV, Yan J, Robinson CV, and Howarth M (2016). Programmable polyproteams built using twin peptide superglues. Proc. Natl. Acad. Sci. USA 113, 1202–1207. 10.1073/pnas.1519214113. [PubMed: 26787909]
59. Bernstein DS, Buter N, Stumpf C, and Wickens M (2002). Analyzing mRNA-protein complexes using a yeast three-hybrid system. Methods 26, 123–141. 10.1016/S1046-2023(02)00015-4. [PubMed: 12054889]
60. Lukas J, Petersen BO, Holm K, Bartek J, and Helin K (1996). Deregulated expression of E2F family members induces S-phase entry and overcomes p16INK4A-mediated growth suppression. Mol. Cell Biol 16, 1047–1057. 10.1128/MCB.16.3.1047. [PubMed: 8622649]
61. Varadi M, Bertoni D, Magana P, Paramval U, Pidruchna I, Radhakrishnan M, Tsenkov M, Nair S, Mirdita M, Yeo J, et al. (2024). AlphaFold Protein Structure Database in 2024: providing structure coverage for over 214 million protein sequences. Nucleic Acids Res. 52, D368–D375. 10.1093/nar/gkad1011. [PubMed: 37933859]
62. Busan S, and Weeks KM (2018). Accurate detection of chemical modifications in RNA by mutational profiling (MaP) with ShapeMapper 2. RNA 24, 143–148. 10.1261/rna.061945.117. [PubMed: 29114018]
63. Darty K, Denise A, and Ponty Y (2009). VARNA: Interactive drawing and editing of the RNA secondary structure. Bioinformatics 25, 1974–1975. 10.1093/bioinformatics/btp250. [PubMed: 19398448]
64. Conesa A, Madrigal P, Tarazona S, Gomez-Cabrero D, Cervera A, McPherson A, Szcześniak MW, Gaffney DJ, Elo LL, Zhang X, and Mortazavi A (2016). A survey of best practices for RNA-seq data analysis. Genome Biol. 17, 13. 10.1186/s13059-016-0881-8. [PubMed: 26813401]
65. Dobin A, Davis CA, Schlesinger F, Drenkow J, Zaleski C, Jha S, Batut P, Chaisson M, and Gingeras TR (2013). STAR: ultrafast universal RNA-seq aligner. Bioinformatics 29, 15–21. 10.1093/bioinformatics/bts635. [PubMed: 23104886]
66. Love MI, Huber W, and Anders S (2014). Moderated estimation of fold change and dispersion for RNA-seq data with DESeq2. Genome Biol. 15, 550. 10.1186/s13059-014-0550-8. [PubMed: 25516281]
67. Vlachos IS, Vergoulis T, Paraskevopoulou MD, Lykokanellos F, Georgakilas G, Georgiou P, Chatzopoulos S, Karagkouni D, Christodoulou F, Dalamagas T, and Hatzigeorgiou AG (2016).

DIANA-mirExTra v2.0: Uncovering microRNAs and transcription factors with crucial roles in NGS expression data. Nucleic Acids Res. 44, W128–W134. 10.1093/nar/gkw455. [PubMed: 27207881]

68. Reimers M, and Carey VJ (2006). Bioconductor: an open source framework for bioinformatics and computational biology. Methods Enzymol. 411, 119–134. 10.1016/S0076-6879(06)11008-3. [PubMed: 16939789]
69. Liao Y, Smyth GK, and Shi W (2014). featureCounts: an efficient general purpose program for assigning sequence reads to genomic features. Bioinformatics 30, 923–930. 10.1093/bioinformatics/btt656. [PubMed: 24227677]
70. Schwartz MR, Luo L, and Berwick M (2019). Sex Differences in Melanoma. Curr. Epidemiol. Rep 6, 112–118. 10.1007/s40471-019-00192-7. [PubMed: 32855900]
71. Wu Y, Zeng J, Roscoe BP, Liu P, Yao Q, Lazzarotto CR, Clement K, Cole MA, Luk K, Baricordi C, et al. (2019). Highly efficient therapeutic gene editing of human hematopoietic stem cells. Nat. Med 25, 776–783. 10.1038/s41591-019-0401-y. [PubMed: 30911135]
72. Martindale JL, Gorospe M, and Idda ML (2020). Ribonucleoprotein Immunoprecipitation (RIP) Analysis. Bio. Protoc 10, e3488. 10.21769/BioProtoc.3488.
73. Martin M. (2011). Cutadapt removes adapter sequences from high-throughput sequencing reads. EMBnet. J 17, 10–12. 10.14806/ej.17.1.200.
74. Yates AD, Achuthan P, Akanni W, Allen J, Allen J, Alvarez-Jarreta J, Amode MR, Armean IM, Azov AG, Bennett R, et al. (2020). Ensembl 2020. Nucleic Acids Res. 48, D682–D688. 10.1093/nar/gkz966. [PubMed: 31691826]
75. Lesurf R, Cotto KC, Wang G, Griffith M, Kasaian K, Jones SJM, Montgomery SB, and Griffith OL; Open Regulatory Annotation Consortium (2016). ORegAnno 3.0: a community-driven resource for curated regulatory annotation. Nucleic Acids Res. 44, D126–D132. 10.1093/nar/gkv1203. [PubMed: 26578589]
76. Georgakilas G, Vlachos IS, Zagganas K, Vergoulis T, Paraskevopoulou MD, Kanellos I, Tsanakas P, Dellis D, Fevgas A, Dalamagas T, and Hatzigeorgiou AG (2016). DIANA-miRGen v3.0: accurate characterization of microRNA promoters and their regulators. Nucleic Acids Res. 44, D190–D195. 10.1093/nar/gkv1254. [PubMed: 26586797]
77. Liu J, Lichtenberg T, Hoadley KA, Poisson LM, Lazar AJ, Cherniack AD, Kovatich AJ, Benz CC, Levine DA, Lee AV, et al. (2018). An Integrated TCGA Pan-Cancer Clinical Data Resource to Drive High-Quality Survival Outcome Analytics. Cell 173, 400–416.e11. 10.1016/j.cell.2018.02.0521. [PubMed: 29625055]
78. Zeng W, Zhang X, Tu X, Guang S, Xiao Y, and Shi Y (2001). Expression and purification of the DNA-binding domain of the human transcription factor E2F1. Protein Expr. Purif 21, 99–104. 10.1006/prep.2000.1346. [PubMed: 11162393]
79. Williams CJ, Headd JJ, Moriarty NW, Prisant MG, Videau LL, Deis LN, Verma V, Keedy DA, Hintze BJ, Chen VB, et al. (2018). MolProbity: More and better reference data for improved all-atom structure validation. Protein Sci. 27, 293–315. 10.1002/pro.3330. [PubMed: 29067766]

Highlights

- The formation of the *SLNCR*-E2F1 complex is crucial for melanoma metastasis
- Disrupting this complex without altering the levels of *either* inhibits melanoma
- E2F1 binds to RNA with faster kinetics and more nucleic acid contacts than to DNA

A **Unbiased TF target enrichment analysis of RNA-seq data from A375 cells overexpressing SLNCR**

Name	Mean	Fold Change	P Value	FDR
SMARCA4	3608	0.81	0.00055	0.030
E2F1	424	0.80	0.00130	0.040
FOSL2	2033	0.85	0.00078	0.033
MZF1	217	0.76	0.0011	0.038

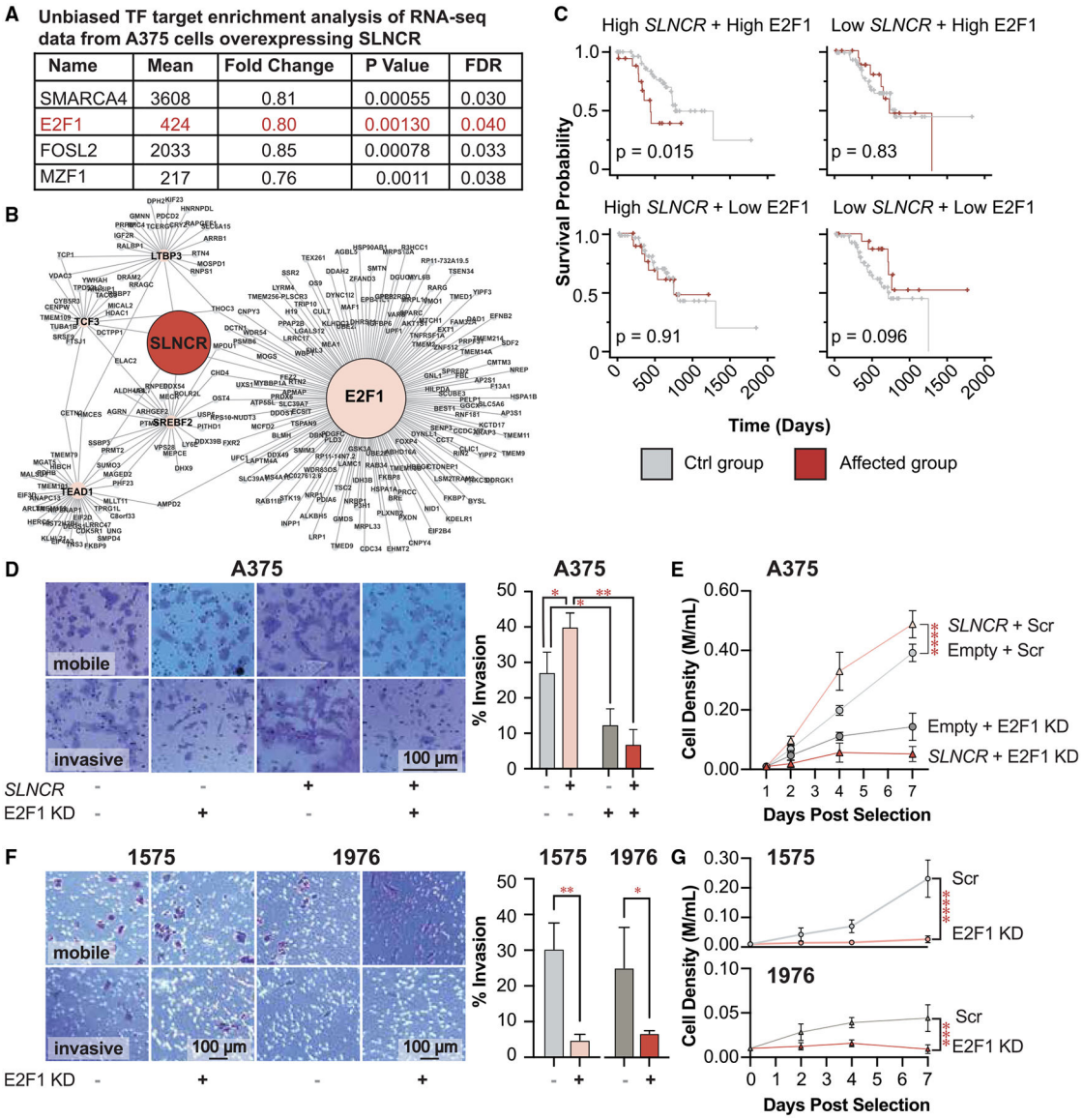

Figure 1. SLNCR and E2F1 co-regulate melanoma-relevant genes

(A) Unbiased TF target enrichment analysis of RNA-seq data from A375 cells overexpressing *SLNCR*.

(B) DATNA of TCGA RNA-seq samples of patients with melanoma.

(C) Kaplan-Meier plots for patients with high levels of *SLNCR* and high levels of E2F1 (top left), high *SLNCR* and low E2F1 (bottom left), low *SLNCR* and high E2F1 (top right), and low *SLNCR* and low E2F1 (bottom right) identified using the TCGA SKCM STAR normalized dataset. Log rank *p* values (*p*) are indicated.

(D) Matrigel invasion assays of A375 cells transfected with *SLNCR* overexpression or empty control plasmid and infected with scramble or E2F1-knockdown (KD) short hairpin RNA (shRNA).

(E) Proliferation assay of A375 transfected as in (D).

(F) Matrigel invasion assays of WM1575 (left) and WM1976 (right) infected with scramble or E2F1-KD shRNA.

(G) Proliferation assay of WM1575 (left) and WM1976 (right) infected as in (F).

In (A)–(G), ****$p < 0.0001$. For (D)–(G), data are represented as mean ± SD. Scale bar represents 100 μm. See also Figure S1 and Table S1.

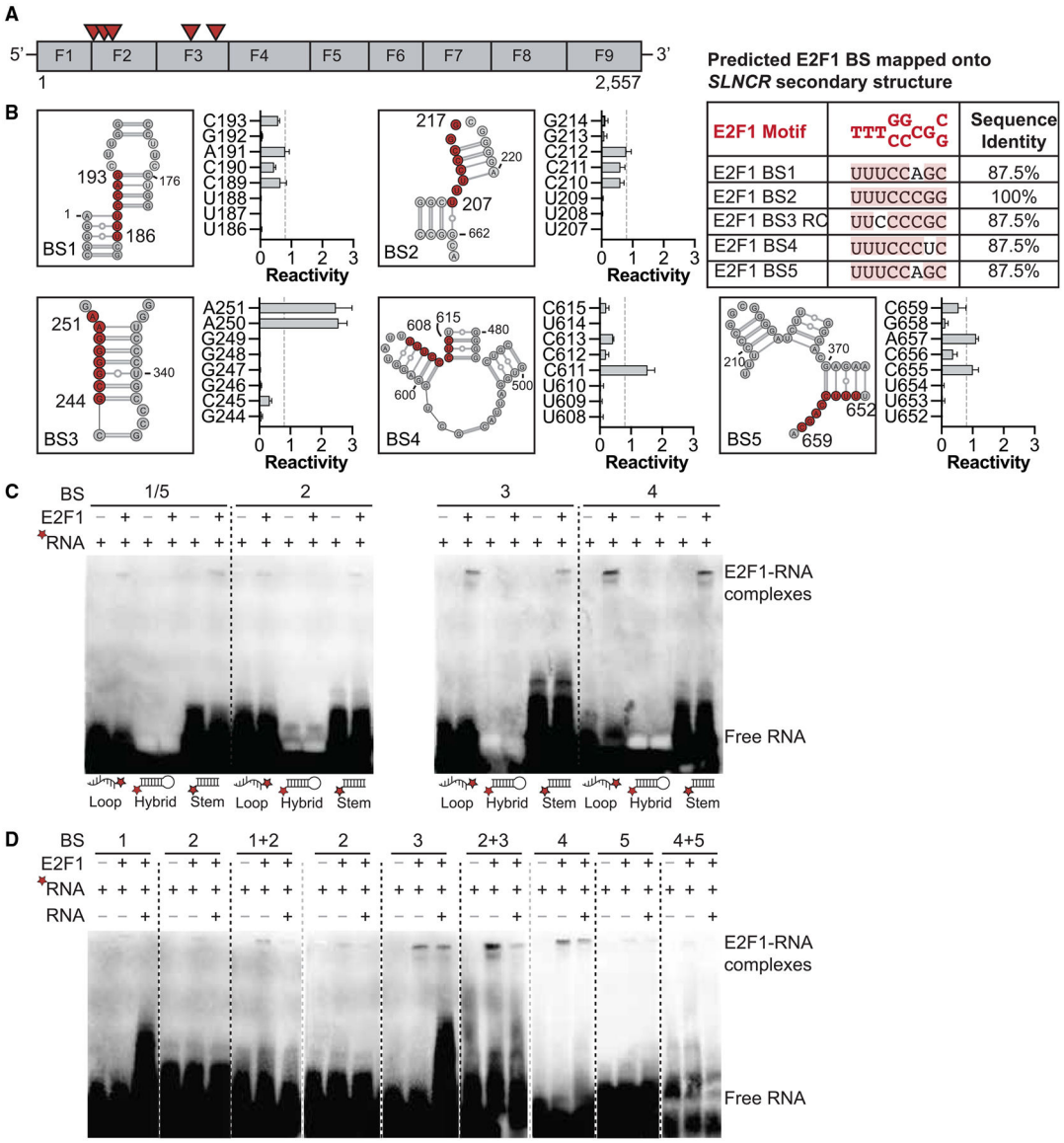

E2F1 Motif	TTTGGCCGCGC	Sequence Identity
E2F1 BS1	UUUCCAGC	87.5%
E2F1 BS2	UUUCCCGG	100%
E2F1 BS3 RC	UUCCCCGC	87.5%
E2F1 BS4	UUUCCCUC	87.5%
E2F1 BS5	UUUCCAGC	87.5%

Figure 2. E2F1 binds to an RNA sequence analogous of the cognate E2F1-binding site on DNA

(A) Schematic presentation of *SLNCR* fragments assayed for E2F1 binding by pairwise Y3H. Predicted E2F1 BSs are marked with red triangles.

(B) Predicted E2F1 BSs mapped onto *SLNCR* secondary structure.

(C) REMSA with biotin-labeled BS1–5 RNA oligonucleotides as single-strand, double-strand, or hybrid fragments, incubated with purified E2F1.

(D) REMSA using biotin-labeled BS1–5 (double-strand), BS1+2, BS2+3, and BS4+5 RNA oligonucleotides with E2F1 with and without competition by unlabeled versions of the same RNA oligonucleotides.

For (C) and (D), gray lines indicate separate gels, and black lines were added for better visualization. See also Figure S2.

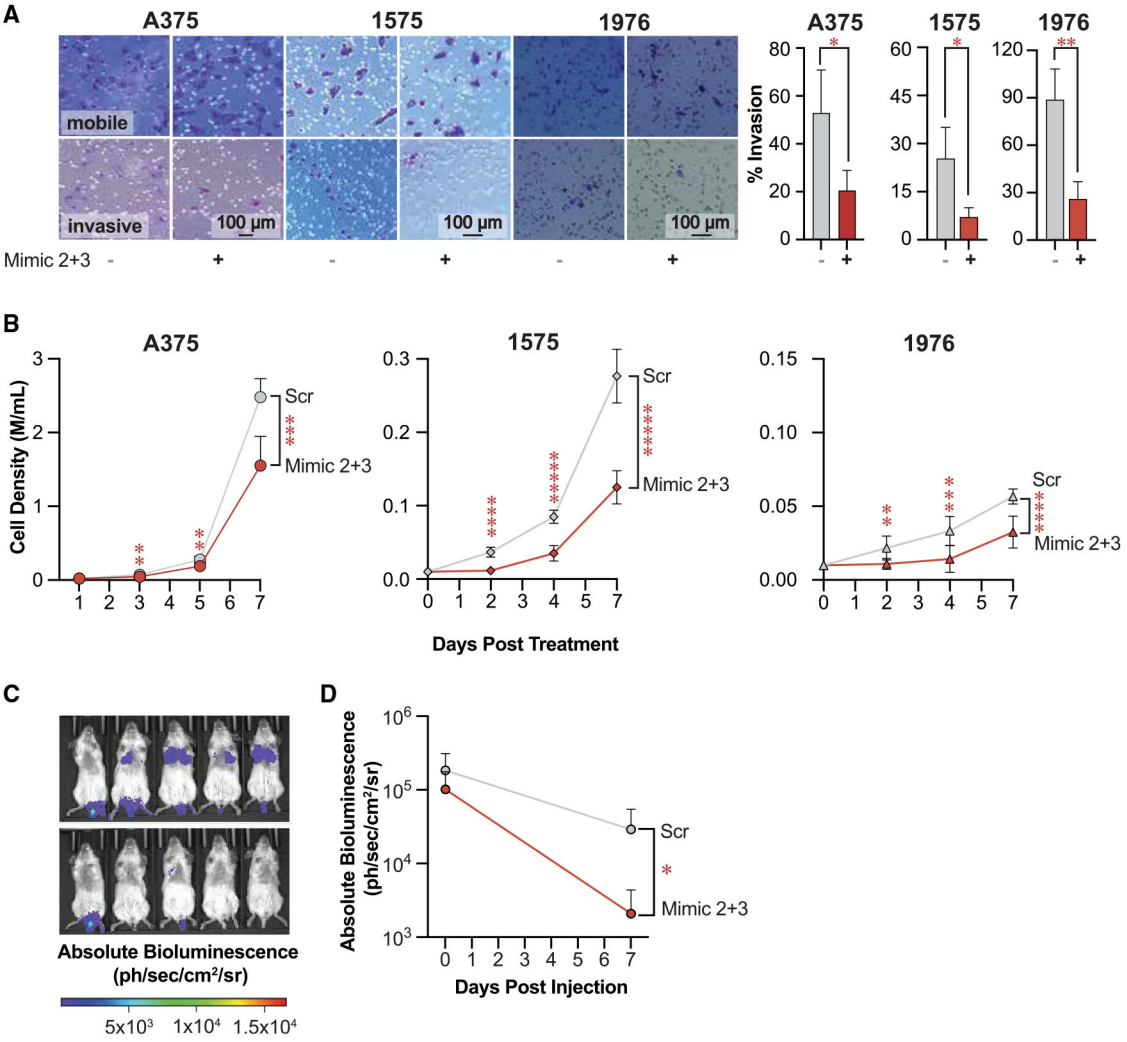

Figure 3. RNA mimic 2+3 oligonucleotide blocks extravasation of melanoma cells in a mouse model of lung extravasation

(A) Matrigel invasion assays of A375 (left), WM1576 (middle), and WM1976 (right) cells transfected with scramble (Scr) or mimic 2+3. Scale bar represents 100 μm.

(B) Proliferation assay of A375 (left), WM1576 (middle), and WM1976 (right) treated with Scr or mimic 2+3. ****$p < 0.0001$.

(C) Bioluminescence images of mice treated with Scr or mimic 2+3-incubated cells.

(D) Tumor growth curve of the mice treated with Scr (gray), and RNA mimic 2+3 oligonucleotide-incubated cells (red).

All data with error bars are presented as mean ± SD. *p* values are defined by unpaired two-tailed t tests. *$p < 0.05$. See also Figure S3.

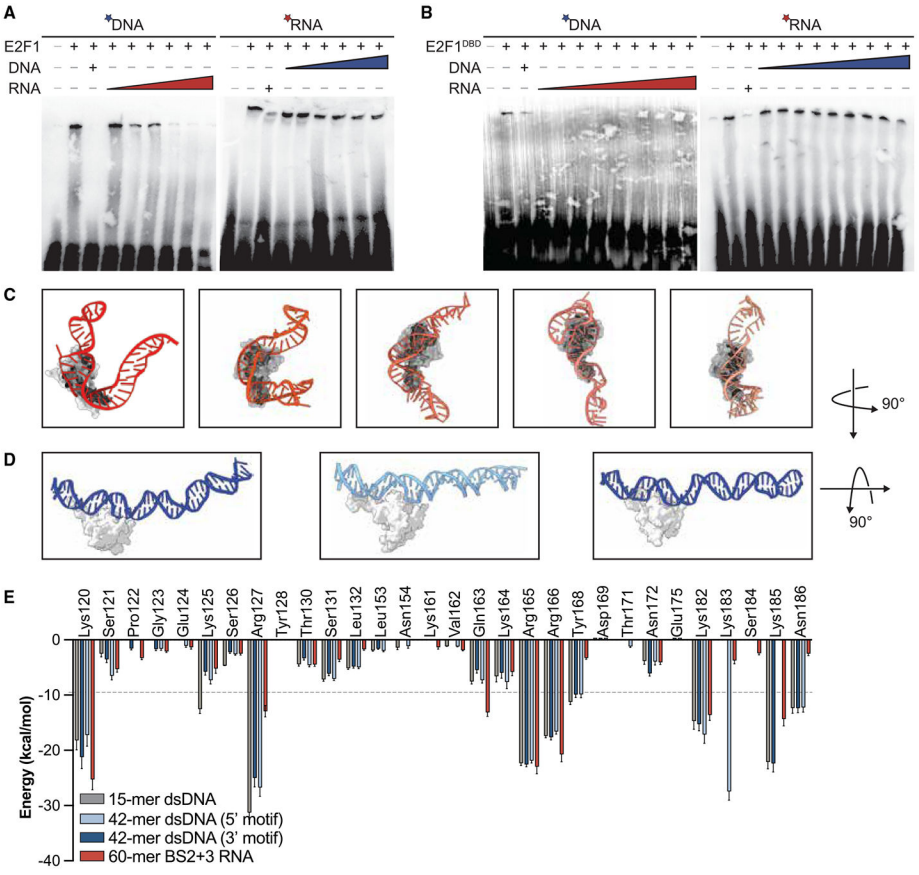

F Number of WT and mutant E2F1^{DBD} interactions at indicated moieties of DNA and RNA oligonucleotides used in MD simulations

	15-mer dsDNA		60-mer BS2+3 RNA	
	Energy (kcal/mol)	No. interacting residues	Energy (kcal/mol)	No. interacting residues
WT	-97.7 ± 3.3	21	-68.7 ± 3.3	24
L132E	-78.4 ± 3.5	22	-57.5 ± 3.5	21
R166H	-79.7 ± 3.5	19	-56.1 ± 3.5	17
42-mer dsDNA (5' motif)	-91.9 +/- 4.3	22		
42-mer dsDNA (3' motif)	-95.0 +/- 4.8	20		

Figure 4. RNA binds to the E2F1 DNA-binding domain (E2F1^{DBD})

(A) REMSA of recombinant E2F1 incubated with biotin-labeled 42-mer dsDNA (left) or 60-mer BS2+3 RNA (right) probes. The labeled 42-mer dsDNA was competed by titrating increasing amounts of unlabeled 60-mer BS2+3 RNA, and vice versa, the labeled 60-mer BS2+3 RNA was competed by titrating increasing amounts of unlabeled 42-mer dsDNA. In each experiment, the third lane from the left has 10 μM unlabeled oligonucleotide of the same species as the labeled nucleotide to show specific binding.

(B) REMSA of recombinant E2F1^{DBD} incubated with biotin-labeled 42-mer dsDNA (left) or 60-mer BS2+3 *SLNCR* RNA (right) probes. The labeled 42-mer dsDNA was competed by titrating increasing amounts of unlabeled BS2+3 RNA, and vice versa, the labeled 60-mer BS2+3 RNA was competed by titrating increasing amounts of unlabeled 42-mer dsDNA. In each experiment, the third lane from left has 18μM unlabeled DNA binding site and 5 μM of unlabeled 60-mer BS2+3 RNA to show specific binding.

(C) Representative structure models of E2F1^{DBD}+60-mer RNA from 5 MD runs.
(D) Representative structure models of E2F1^{DBD}+42-mer dsDNA from 3 MD runs.
(E) Averaged residue interaction energies of E2F1^{DBD} with the 15-mer reference dsDNA (gray), the 42-mer DNA 5′ motif (light blue), the 42-mer dsDNA 3′ motif (dark blue), and 60-mer RNA (red) calculated by MMGBSA. Gray dashed line indicates −9.8 kcal/mol threshold for strong interactions.
(F) Number of wild-type (WT) and mutant E2F1^{DBD} interactions at the base, phosphate, and sugar moieties of 15-mer dsDNA, 42-mer dsDNA 5′ and 3′ motifs, and 60-mer BS2+3 RNA.
See also Figure S4 and Videos S1, S2, S3, S4, S5, S6A, S6B, and S7.

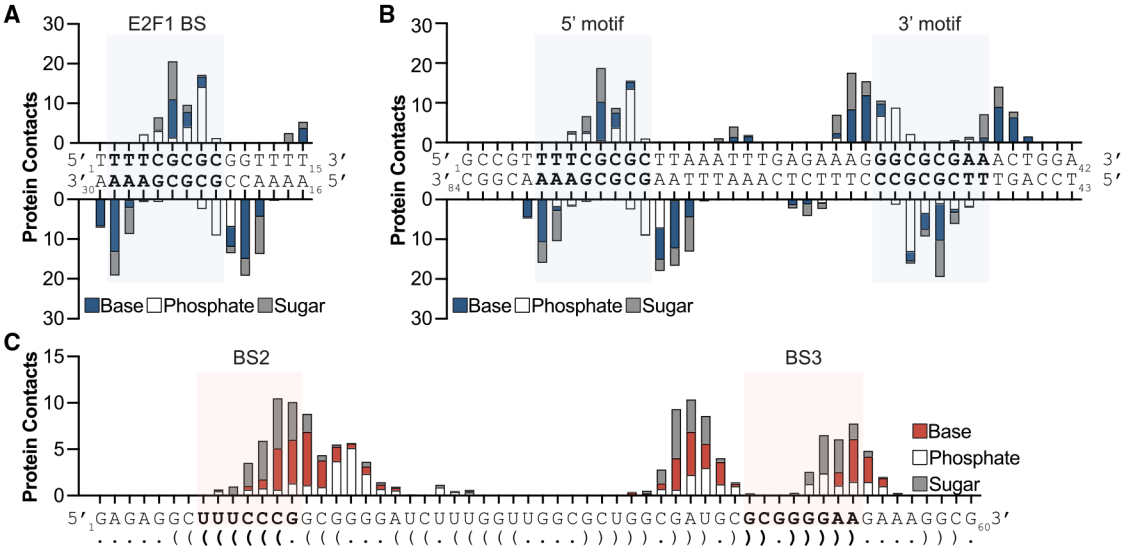

D **Summary of the protein contacts with indicated moieties in each MD model**

Nucleic acid model	Number of interactions			
	Base	Phosphate	Sugar	Total
15-mer dsDNA	66	46	47	160
42-mer dsDNA (5′ motif)	59	48	47	155
42-mer dsDNA (3′ motif)	60	48	50	159
60-mer BS2+3 RNA	47	38	46	133

Figure 5. Molecular dynamics simulations of the interaction between E2F1 and nucleic acids

(A–C) Amount of protein contacts per nucleotide calculated by MMGBSA at base, phosphate, or sugar moieties.

(A) Calculated protein contacts for the E2F1^{DBD}+15-mer dsDNA model. The top graph shows contacts with the sense strand (5′ to 3′), and the bottom graph shows protein contacts with the antisense strand (3′ to 5′). The E2F1 BS is shaded.

(B) Calculated protein contacts for the E2F1^{DBD}+42-mer dsDNA model. The top graph shows contacts with the sense strand (5′ to 3′), and the bottom graph shows protein contacts with the antisense strand (3′ to 5′). The 5′ and 3′ motifs are shaded.

(C) Calculated protein contacts for the E2F1^{DBD}+60-mer BS2+3 RNA model. Base-pairing interactions as predicted by RNAFold are shown as dot-and-bracket annotations below the sequence. BS2 and BS3 are shaded.

(D) Table summarizing the protein contacts with base, phosphate, and sugar moieties in each MD model.

See also Figure S5.

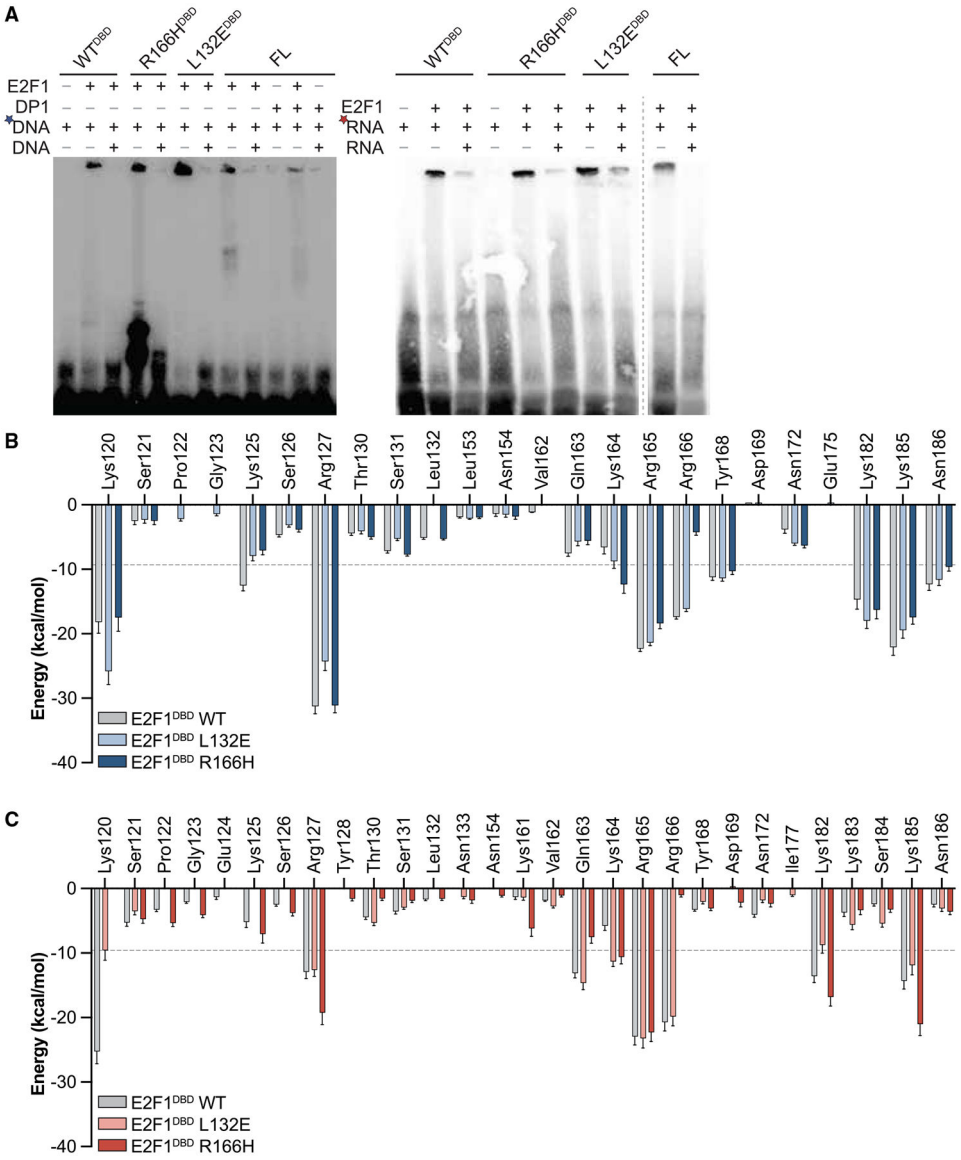

Figure 6. R166H and L132E mutations did not affect the overall binding affinity of E2F1

(A) REMSA of γ-P-labeled 42-mer dsDNA (left) or biotin-labeled 60-mer BS2+3 RNA, (right) incubated with WT or mutant (R166H or L132E) E2F1^{DBD} or full-length E2F1 and DP1.

(B and C) Averaged residue interaction energies calculated by MMGBSA of WT and mutant E2F1^{DBD} with 15-mer reference dsDNA (B) or 60-mer BS2+3 RNA (C). Gray dashed line indicates −9.8 kcal/mol threshold for strong interactions. WT systems are first presented in Figure 4E and are re-plotted here for comparison with the mutants.

See also Figure S6.

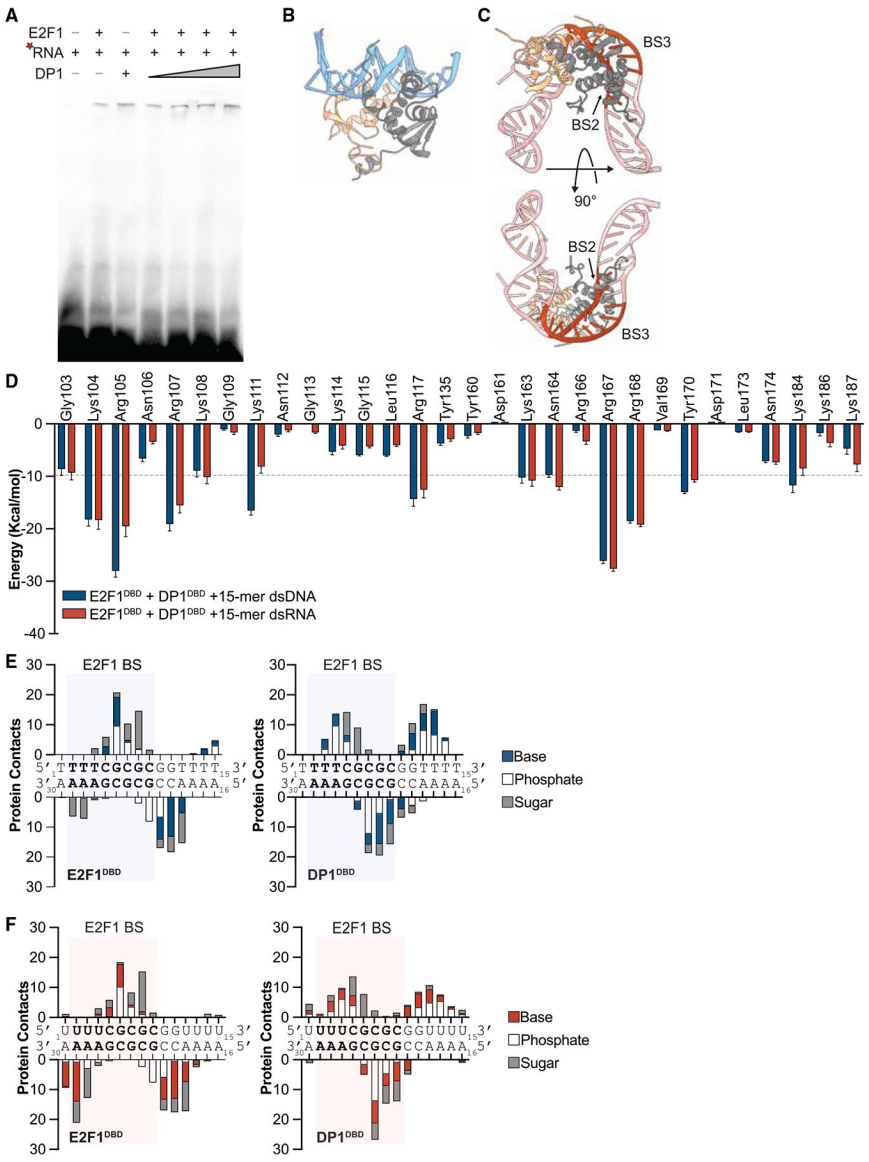

Figure 7. Molecular dynamics simulations indicate that DP1 and RNA binding to E2F1 are mutually exclusive

(A) REMSA using biotin-labeled 60-mer BS2+3 RNA incubated with recombinant E2F1 or DP1 or both with increasing amounts of DP1.

(B) Representative structure from 3 independent simulations of E2F1^{DBD}+DP1^{DBD}+15-mer dsDNA showing the arrangement of the ternary system. E2F1 (salmon), DP1 (gray), and 15-mer reference dsDNA (blue).

(C) Model structure of the E2F1^{DBD}+60-mer *SLNCR* RNA with DP1 docked to fit the interaction interface of E2F1 (salmon), DP1 (gray), and RNA (orange).

(D) Averaged residue interaction energies of DP1^{DBD} calculated using MMGBSA of the E2F1^{DBD} +DP1^{DBD} +15-mer dsDNA and E2F1^{DBD}+DP1^{DBD}+15-mer dsRNA models. The RNA in the latter system was created by directly converting 15-mer dsDNA (by adding O2′) to get a 15-mer dsRNA backbone. Gray dashed line indicates −9.8 kcal/mol threshold for strong interactions.

(E) Amount of protein contacts per nucleotide calculated by MMGBSA of the $E2F1^{DBD}$+$DP1^{DBD}$+15-mer dsDNA model at base, phosphate, or sugar moieties contributed by $E2F1^{DBD}$ (left) and those contributed by $DP1^{DBD}$ (right). The top graphs show contacts with the sense strand (5′ to 3′), and the bottom graphs show protein contacts with the anti-sense strand (3′ to 5′). The E2F1 BS is shaded.

(F) Amount of protein contacts per nucleotide calculated by MMGBSA of the $E2F1^{DBD}$+$DP1^{DBD}$+15-mer dsRNA model as described in (E).

See also Figure S7 and Videos S8 and S9.

Table 1.

MD systems

System	Na^+	Cl^-	Water	Total atoms
$E2F1^{DBD}$	23	27	12,533	39,029
E2F1-$R166H^{DBD}$	23	26	12,533	39,021
E2F1-$L132E^{DBD}$	23	26	12,533	39,024
$E2F1^{DBD}$+15-mer dsDNA	57	31	16,722	52,593
E2F1-$R166H^{DBD}$+15-mer dsDNA	57	30	16,722	52,585
E2F1-$L132E^{DBD}$+15-mer dsDNA	57	30	16,722	52,588
$E2F1^{DBD}$+60-mer RNA	156	101	55,372	169,703
E2F1-$R166H^{DBD}$+60-mer RNA	156	100	55,372	169,695
E2F1-$L132E^{DBD}$+60-mer RNA	156	100	55,372	169,698
$E2F1^{DBD}$+DP1	33	43	18,152	57,554
$E2F1^{DBD}$+DP1+15-mer dsDNA	57	37	20,595	65,860
$E2F1^{DBD}$+DP1+15-mer dsRNA	57	37	20,595	65,866
$E2F1^{DBD}$+42-mer dsDNA	196	118	64,943	199,188
42-mer dsDNA	108	26	14,184	45,351
60-mer RNA	108	49	26,529	81,694
Binding site 1 stem	63	26	14,202	43,909
Binding site 1 loop	71	34	18,273	56,130
Binding site 1 hybrid	43	22	12,092	37,041
Binding site 2 stem	64	27	14,435	44,612
Binding site 2 loop	71	34	18,273	56,128
Binding site 2 hybrid	50	24	13,010	39,971
Binding site 3 stem	64	24	14,431	44,602
Binding site 3 loop	71	27	18,291	56,183
Binding site 4 stem	64	34	14,499	44,802
Binding site 4 loop	54	28	14,961	45,811
Binding site 4 hybrid	42	21	11,414	34,999
Binding site 1+2	103	44	23,713	73,203
Binding site 2+3	108	49	26,529	81,694

System	Na^+	Cl^-	Water	Total atoms
Binding site 4+5	120	59	31,829	97,614

Table 2.

Oligonucleotides used in this study

Name	Primer pair	Purpose
SLNCR	5′-GGACCCCTTAACGTGGATTAC-3′	qPCR
	5′-AAATACCTCCAGCTTGGCG-3′	
B-actin	5′-AACTTCTACAATGAGCTGCG-3′	qPCR
	5′-CCTGGATAGCAACGTACATGG-3′	
E2F1	5′-ACGTGACGTGTCAGGACCT-3′	qPCR
	5′-GATCGGGCCTTGTTTGCTCTT-3′	
	5′-AATTCAAAAAAGCTGGACCACCTGATG	
	AATACTCGAGTATTCATCAGGTGGTCCAGCT-3′	
E2F1 shRNA	5′-CCGGACCTCTTCGACTGTGACTTTGCTC	Cloning
	GAGCAAAGTCACAGTCGAAGAGGTTTTTTG-3′	
	5′-AATTCAAAAAACCTCTTCGACTGTGACTT	
	TGCTCGAGCAAAGTCACAGTCGAAGAGGT-3′	
Binding site 1 double stranded	5′-AUCGAUUUCCAGCUCGAUCGAUCGAGCUGGAAAUCGAU-3′	REMSA
Binding site 1 single stranded	5′-UCGAUCGAUCGAUCUUUCCAGCAGCUUCGAUCGAUCGA-3′	REMSA
Binding site 1 hybrid	5′-CCACAGCGCUUUCCAGCUGUGG-3′	REMSA
Binding site 2 double stranded	5′-AUCGAUUUCCCGCUCGAUCGAUCGAGCGGGAAAUCGAU-3′	REMSA
Binding site 2 single stranded	5′-UCGAUCGAUCGAUCUUUCCCGCAGCUUCGAUCGAUCGA	REMSA
Binding site 2 hybrid	5′-CGCUUUCCCGGCUAGCCAAAGAAAGCG-3′	REMSA
Binding site 3 double stranded	5′-AUCGAUUCCCCGCUCGAUCGAUCGAGCGGGGAAUCGAU-3′	REMSA
Binding site 3 single stranded	5′-UCGAUCGAUCGAUCUUCCCCGCAGCUUCGAUCGAUCGA-3′	REMSA
Binding site 4 double stranded	5′-AUCGAUUUCCCUCUCGAUCGAUCGAGAGGGAAAUCGAU-3′	REMSA
Binding site 4 single stranded	5′-UCGAUCGAUCGAUCUUUCCCUCAGCUU-3′	REMSA
Binding site 4 hybrid	5′-GUCGAGGUAUUUUUCCCUCGAC-3′	REMSA
Binding site 1+2	5′-ACGAUCCGCCUUCAGCGCUUUCCAGCUUGG	REMSA
	CAGAGAGGCUUUCCCGGCGGGGAUCUUUGG-3′	
Binding site 2+3	5′-GAGAGGCUUUCCCGGCGGGGAUCUUUGGUU	REMSA/proliferation/invasion/luciferase assays, MD simulation
	GGCGCUGGCGAUGCGCGGGGAAGAAAGGCG-3′	
Binding site 4+5	5′-GUAUUUUUCCCUCUCCACCCUGGUCUUCUCCU	REMSA
	GUAACGUGUGGCCGCCUUUUCCAGCACGGC-3′	

Name	Primer pair	Purpose
2XE2F1_DNA_BS (dsDNA 42)	5′-GCCGTTTTCGCGCTTAAATTTGAGAAAGGGCGCGAAACTGGA-3′	EMSA, MD simulation
	5′-TCCAGTTTCGCGCCCTTTCTCAAATTTAAGCGCGAAAACGGC-3′	
15-mer dsDNA	5′-TTTTCGCGCGGTTTT-3′	MD simulation
	5′-AAAACCGCGCGAAAA-3′	
15-mer dsRNA	5′-UUUUCGCGCGGUUUU-3′	MD simulation
	5′-AAAACCGCGCGAAAA-3′	
Scr (AUM*block* oligo)	5′-CCTTCCCTGAAGGTTCCTCC-3′	REMSA, proliferation, invasion assay
RNA Mimic 2+3 (AUM*block* oligo)	5′-GAGAGGCTTTCCCGGCGGGGATCTTTGGTTGGC	REMSA, proliferation, invasion assay
	GCTGGCGATGCGCGGGGAAGAAAGGCG-3′	
E2F1-DBD-f/r	5′-CCTCTAGAAATAATTTTGTTTAACTTTAAG-3′	Cloning
	5′-GTTAGCAGCCGGATCTCAGTGGTGGTGGTGG	
	TGGTGTCACTCGAGGTGGCTGCCC-3′	
SLNCR fragment 1	5′-CTGGTATCCAGAGGACGCG-3′	DMS-probing
	5′-GAGAAGAGGTCGTGGGTCTTC-3′	
SLNCR fragment 2	5′-GACCTCCGCGAGTCTGG-3′	DMS-probing
	5′-GTGGATCAGTCCTTCCCATCCC-3′	
SLNCR fragment 3	5′-GAAGACCCACGACCTCTTCTC-3′	DMS-probing
	5′-GGCACAGCAGACATGGGAG-3′	
SLNCR fragment 4	5′-CTCTTCCCCCTCCCTGTCC-3′	DMS-probing
	5′-GCTCTGACTCTGCATTTGGAC-3′	
SLNCR reverse transcription	5′-CCGGCTGGAAGATAATGGAGC-3′	DMS-probing
E2F1-HiBiT-ampl f/r	5′-TTCATCAGCCTTTCCCCACC-3′	RNA-IP cell line generation
	5′-CTCCTTCCCTTCCTGGCTTG-3′	
E2F1ampl-seqr	5′-TCAGCCTCCTAGCGGTAG-3′	RNA-IP cell line generation
E2F1-g2 (crRNA)	rCrArCrCrCrCrCrUrGrGrArUrUrUrCrUrGrArCr GrUrUrUrUrArGrArGrCrUrArUrGrCrU	RNA-IP cell line generation
ssODN2_E2F1-Cterm_5arm-Val-Ser-HiBiT-3arm	5′-A*C*CACTTCGGCCTCGAGGAGGGCGAGGGCATCAGAGACC TCTTCGACTGTGACTTTGGGGACCTCACCCCCCTGGATTTCGTC TCCGTGAGCGGCTGGCGGCTGTTCAAGAAGATTAGCTGACAGG GCTTGGAGGGACCAGGGTTTCCAGAGATGCTCACCTTGTCTCTG CAGCCCTGGAGCCCCCTGTCCCTGGCC*−3′	RNA-IP cell line generation

KEY RESOURCES TABLE

REAGENT or RESOURCE	SOURCE	IDENTIFIER
Antibodies		
Anti-E2F1	Cell Signaling Technology	Cat# 3742; RRID:AB_2096936
Anti-Cyclophilin B (D1V5J)	Cell Signaling Technology	Cat # 43603; RRID:AB_2799247
Monoclonal Anti HiBiT antibody	Promega	Cat# N7200; RRID: AB_3665694
Normal mouse IgG antibody	Millipore Sigma	Cat# CS200621
Bacterial and virus strains		
Chemocompetent 5-α cells	New England Biolabs	Cat# C2987H
Chemocompetent BL21(DE3) pLysS cells	Life Technologies	Cat# C606010
Chemicals, peptides, and recombinant proteins		
5% Mini-PROTEAN® TBE Gel, 12 well, 20 μL	BioRad	Cat# 4565015
6% DNA retardation TBE Gel, 10 well, 30 μL	Life Technologies	Cat# EC6365BOX
12% Mini-PROTEAN® TGX Precast Protein Gels	BioRad	Cat# 4561045EDU
Amersham Hybond-N+	GE Healthcare Lifesciences	Cat# RPN203B
GIBCO FBS	Thermo Fisher Scientific	Cat# 26140079
GIBCO Trypsin-EDTA (0.05%), phenol red	Thermo Fisher Scientific	Cat# 25300054
Nitrocellulose 0.2 μm membrane	BioRad	Cat# 1620146
GIBCO DMEM, high glucose, pyruvate	Thermo Fisher Scientific	Cat# 11995073
Recombinant Human E2F1 protein	Abcam	Cat# ab82207-5ug
$E2F1^{DBD}$	This Paper	N/A
3-Amino-1,2,4-triazole (3AT)	Millipore Sigma	Cat# A8056-100G
Fisher HealthCare PROTOCOL Hema 3 Fixative and Solutions	Thermo Fisher Scientific	Cat# 23123869
Amicon Ultracentrifugation filter 10 kDa	Millipore Sigma	Cat# UFC9010
5X Novex TBE loading dye	Life Technologies	Cat# LC6678
NovexÂ® TBE Running Buffer (5X)	Life Technologies	Cat# LC6675
Dimethyl sulfoxide	Millipore Sigma	Cat# D2650
Dimethyl Sulfate	Millipore Sigma	Cat# D186309
TRIzol	Life Technologies	Cat# 15596026
TURBO™ DNase	Life Technologies	Cat# AM2238
Proteinase K, recombinant	ThermoFisher Scientific	Cat#EO0492
Induro reverse transcriptase	New England Biolabs	Cat# M0681
ATP, [gamma-32P], 3000 Ci/mmol 10 mCi/mL, 250 μCi	Perkin Elmer	Cat# BLU002A250UC
GIBCO β-mercaptoethanol	Thermo Fisher Scientific	Cat# 21985023
PBS 1X W/O CA MG 500 ML	Thermo Fisher Scientific	Cat# MT21040CV
NONFAT DRY MILK/500G	Thermo Fisher Scientific	Cat# NC9121673
TBS with Tween™ (TBST), 20X Solution, Molecular Biology Grade, Ultrapure, Thermo Scientific Chemicals	Thermo Fisher Scientific	Cat# J77500.K2
10x Tris/Glycine/SDS Electrophoresis Buffer	BioRad	Cat# 1610772EDU

REAGENT or RESOURCE	SOURCE	IDENTIFIER
10x Tris/Glycine	BioRad	Cat# 1610734EDU
2x Laemmli Sample Buffer	BioRad	Cat# 1610737
Lipofectamine® 2000	Life Technologies	Cat# 11668027
Puromycin	Thermo Fisher Scientific	Cat# A1113803
Gibco Trypsin-EDTA (0.05%), phenol red	Thermo Fisher Scientific	Cat# 25300054
SphI-HF	New England Biolabs	Cat# R3182S
SmaI	New England Biolabs	Cat# R0141S
T4 DNA Ligase	New England Biolabs	Cat# M0202S
cOmplete™, Mini, EDTA-free Protease Inhibitor Cocktail, Roche	Millipore Sigma	Cat# 11836170001
Dynabeads	Invitrogen	Cat#10003D
Critical commercial assays		
LightShift Chemiluminescent RNA EMSA (REMSA) Kit	Thermo Fisher Scientific	Cat# 20148
RNeasy® plus Mini Kit	Qiagen	Cat# 74134
SuperScript™ III Reverse Transcriptase	Invitrogen	Cat# 18080085
SsoAdvanced Universal SYBR® Green SuperMix	BioRad	Cat# 1725271
Zymogen DNA Clean & Concentrator®-5 Kit	Zymo Research	Cat# D4013
Gibson Assembly® Master Mix	New England Biolabs	Cat# E2611S
Corning BioCoat™ Matrigel Invasion Chambers with 8.0 μm PET Membrane	Westnet Inc.	Cat# 354480
Corning BioCoat™ Control Inserts with 8.0 μm PET Membrane	Westnet Inc.	Cat# 354578
Deposited data		
A375 RNA-seq	This study. NCBI's Gene Expression Omnibus	GEO: GSE270372
cBioPortal	Cerami et al., 2012; Gao et al., 2013	https://www.cbioportal.org/
The Cancer Genome Atlas		https://xenabrowser.net/datapages/
Protein DataBank	PDB: 1CF7	https://www.wwpdb.org/
Code for Disease Associated Transcriptional Network Analysis (DATNA)	This study, Github	https://github.com/kushanishah/slncr-e2f1-melanoma
Human reference genome NCBI build 38, GRCh38	Genome Reference Consortium	http://www.ncbi.nlm.nih.gov/projects/genome/assembly/grc/human/
Experimental models: Cell lines		
A375	American Type Culture Collection	Cat# ATCC® CRL-1619; RRID: CVCL_0132
A375-Luc2	American Type Culture Collection	Cat# ATCC® CRL-1619-LUC2; RRID: CVCL_UR32
HEK293T	Gift Ronny Drapkin	
WM1575	Gift Wistar Institute	
WM1976	Gift Wistar Institute	
Experimental models: Organisms/strains		
Mice: NOD.Cg-Prkdcscid Il2rgtm1Wjl/SzJ (Females)	The Jackson Laboratory	Cat# 005557; RRID: IMSR_JAX:005557
Saccharomyces cerevisiae strain YLW3/YBZ1 *(MATalpha trp1-1 leu2-3,112 ura3-52*	Hook et al.[55]	

REAGENT or RESOURCE	SOURCE	IDENTIFIER
his3-200 ade2 LYS2::(LexAop)-HIS3, URA3::(lexAop)-lacZ, LexA-MCP (N55K) (TRP1) gal4D::KANMX cyh2r)		
Saccharomyces cerevisiae strain Y8800 *(MATa trp1-901 leu2-3,112 ura3-52 his3-200 ade2-101 gal4D gal80D cyh2r GAL2::ADE2 GAL1::HIS3@LYS2 GAL7::LacZ@met2)*	James et al.[56]	
Oligonucleotides		
All oligonucleotides	See Table 2	N/A
Recombinant DNA		
SLNCR overexpression plasmid in pcDNA3.1/Puro-CAG	This study	N/A
pcDNA3.1/Puro-CAG-VSFP-CR	Lam et al.[57]	Addgene Cat# 40257; RRID: Addgene_40257
pET28a SpyCatcher-SnoopCatcher	Veggiani et al.[58]	Addgene Cat# 72324; RRID: Addgene_72324
pIIIA-MS2-1	Bernstein et al.[59]	Addgene Cat #220631; RRID: Addgene_220631
pCMVHA E2F1	Lukas et al.[60]	Addgene Cat #24225; RRID: Addgene_24225
Software and algorithms		
DATNA R code	This study	Zenodo at https://doi.org/10.5281/zenodo.15008289
GraphPad Prism version 10.00 for MAC	GraphPad Software	https://www.graphpad.com/; RRID: SCR_002798
AlphaFold DB	Varadi et al.[61]	https://alphafold.ebi.ac.uk
Amber20		https://ambermd.org/; RRID: SCR_018497
ShapeMapper 2	Busan & Weeks[62]	https://webshare.oasis.unc.edu/weeksgroup/shapemapper-2.1.3.tar.gz
RNAFold (v6.4)	Mathews[19]; Reuters and Mathews[20]	http://rna.tbi.univie.ac.at//cgi-bin/RNAWebSuite/RNAfold.cgi; RRID: SCR_024427
VARNA	Darty et al.[63]	http://varna.lri.fr; RRID: SCR_024373
FastQC (v0.11.5)		https://www.bioinformatics.babraham.ac.uk/projects/fastqc/; RRID: SCR_014583
Cutadapt (v2.5)	Martin <https://journal.embnet.org/index.php/embnetjournal/article/view/200/479>; Conesa et al.[64]	https://cutadapt.readthedocs.io/en/v2.5/installation.html; RRID: SCR_011841
STAR (v2.7.3a)	Dobin et al.[65]	http://code.google.com/p/rna-star/; RRID: SCR_004463
DESeq2 (v1.24.0)	Love et al.[66]	https://bioconductor.org/packages/release/bioc/html/DESeq2.html; RRID: SCR_015687
DIANA-mirExTra (v2.0)	Vlachos et al.[67]	http://carolina.imis.athena-innovation.gr/mirextra/; RRID: SCR_017498
Bioconductor	Reimers and Carey[68]	http://www.bioconductor.org/; RRID: SCR_006442
featureCounts (Subread 1.6.2)	Liao et al.[69]	http://bioinf.wehi.edu.au/featureCounts/; RRID: SCR_012919
Xena GDC		https://xenabrowser.net/datapages/; RRID: SCR_018938
R (R 3.6.0)		http://www.r-project.org/; RRID: SCR_001905
survival (v3.5-7)		https://CRAN.R-project.org/package=survival; RRID: SCR_021137
survminer (v0.4.9)		https://rdocumentation.org/packages/survminer/versions/0.4.9; RRID: SCR_021094
ggsurvfit (v0.2.0)		https://CRAN.R-project.org/package=ggsurvfit; RRID: SCR_025045